

# Ly $\alpha$ emission-line reconstruction for high- $z$ QSOs

Bradley Greig,<sup>1\*</sup> Andrei Mesinger,<sup>1</sup> Ian D. McGreer,<sup>2</sup> Simona Gallerani<sup>1</sup>  
and Zoltán Haiman<sup>3</sup>

<sup>1</sup>*Scuola Normale Superiore, Piazza dei Cavalieri 7, I-56126 Pisa, Italy*

<sup>2</sup>*Steward Observatory, The University of Arizona, 933 North Cherry Avenue, Tucson, AZ 85721-0065, USA*

<sup>3</sup>*Department of Astronomy, Columbia University, 550 West 120th Street, New York, NY 10027, USA*

Accepted 2016 December 7. Received 2016 December 7; in original form 2016 May 30

## ABSTRACT

We introduce an intrinsic Ly $\alpha$  emission-line profile reconstruction method for high- $z$  quasars (QSOs). This approach utilises a covariance matrix of emission-line properties obtained from a large, moderate- $z$  ( $2 \leq z \leq 2.5$ ), high signal to noise ( $S/N > 15$ ) sample of BOSS QSOs. For each QSO, we complete a Monte Carlo Markov Chain fitting of the continuum and emission-line properties and perform a visual quality assessment to construct a large data base of robustly fit spectra. With this data set, we construct a covariance matrix to describe the correlations between the high-ionization emission lines Ly $\alpha$ , C IV, Si IV + O IV] and C III], and find it to be well approximated by an  $N$ -dimensional Gaussian distribution. This covariance matrix characterizes the correlations between the linewidth, peak height and velocity offset from systemic while also allowing for the existence of broad- and narrow-line components for Ly $\alpha$  and C IV. We illustrate how this covariance matrix allows us to statistically characterize the intrinsic Ly $\alpha$  line solely from the observed spectrum redward of 1275 Å. This procedure can be used to reconstruct the intrinsic Ly $\alpha$  line emission profile in cases where Ly $\alpha$  may otherwise be obscured. Applying this reconstruction method to our sample of QSOs, we recovered the Ly $\alpha$  line flux to within 15 per cent of the measured flux at 1205 Å (1220 Å)  $\sim$ 85 (90) per cent of the time.

**Key words:** quasars: absorption lines – quasars: emission lines – quasars: general – cosmology: observations – cosmology: theory.

## 1 INTRODUCTION

The ability to measure the intrinsic spectrum of quasars (QSOs) plays an important role in astrophysics. Resolving individual emission-line profiles can enable the detailed study of both the central supermassive black hole (SMBH) and the internal structure within the SMBH-powered accretion disc (through reverberation mapping e.g. Blandford & McKee 1982; Peterson 1993 or the virial method e.g. Kaspi et al. 2000; Peterson et al. 2004; Vestergaard & Peterson 2006). On cosmological scales, the relative strength (or lack thereof) of the emission profiles and spectral slopes of the QSO continuum can be used to yield insights into the thermal and ionization state of the intergalactic medium (IGM) through studies of the QSO proximity zone (e.g. Mesinger & Haiman 2004; Wyithe & Loeb 2004; Fan et al. 2006; Bolton & Haehnelt 2007a; Mesinger & Haiman 2007; Carilli et al. 2010; Calverley et al. 2011; Wyithe & Bolton 2011; Schroeder, Mesinger & Haiman 2013).

The key ingredient for using QSOs to explore the IGM is observing the intrinsic ultraviolet (UV) emission. Thermal emission from the accretion disc peaks in UV, which then interacts with surrounding neutral hydrogen and recombines two-thirds of the time into Ly $\alpha$  photons (rest-frame  $\lambda_{\text{Ly}\alpha} = 1215.67$  Å) to produce a prominent Ly $\alpha$  emission profile. However, owing to the large scattering cross-section of Ly $\alpha$  photons, neutral hydrogen column densities of  $N_{\text{H I}} > 10^{18} \text{ cm}^{-2}$  are sufficient for Ly $\alpha$  to enter into the strong absorption regime. In the case of the IGM, even minute traces ( $\sim$  few per cent) of intervening neutral hydrogen along the line of sight are capable of scattering Ly $\alpha$  photons away from the observer.

At  $z \lesssim 3$ , the IGM is, on average, very highly ionized except in dense self-shielded clumps (e.g. Fan et al. 2006; McGreer, Mesinger & D’Odorico 2015; Planck Collaboration XIII 2015; Planck Collaboration XLVI 2016; Planck Collaboration XLVII 2016). Typically, at these redshifts, the resonant scattering and absorption of Ly $\alpha$  photons occurs only due to diffuse amounts of neutral hydrogen that appear blueward of Ly $\alpha$  ( $\lambda < \lambda_{\text{Ly}\alpha}$ ) as a series of discrete narrow absorption features, known as the Ly $\alpha$  forest (Rauch 1998). More problematic for measuring the intrinsic Ly $\alpha$  emission line are larger

\*E-mail: [bradley.greig@sns.it](mailto:bradley.greig@sns.it)

neutral column density absorbers such as Lyman-limit systems and damped Ly $\alpha$  absorbers (DLAs). In the case of DLAs, with column densities of  $N_{\text{H I}} > 10^{20} \text{ cm}^{-2}$ , not only do these systems lead to completely saturated absorption, but they are also sufficiently dense to allow Ly $\alpha$  absorption within the Lorentzian wings. If these DLAs are located sufficiently close to the source QSO, absorption in the wings can significantly affect the intrinsic Ly $\alpha$  emission profile. Furthermore, associated strong absorbers intrinsic to the host QSO environment itself can additionally impact the Ly $\alpha$  line emission (Shen & Ménard 2012).

At  $z > 6$ , the IGM becomes increasingly neutral and the Ly $\alpha$  forest gives way to completely dark (absorbed) patches (e.g. Barkana 2002; Gallerani et al. 2008; Mesinger 2010; McGreer et al. 2015). Once the IGM itself obtains a sufficiently large column density, it too begins to absorb Ly $\alpha$  in the Lorentzian wings of the scattering cross-section, referred to as IGM damping wing absorption (Miralda-Escudé 1998). In principle, through the detection of the IGM damping wing imprint from the Ly $\alpha$  emission spectra of high- $z$  QSOs one is able to provide a direct measurement of the neutral fraction of the IGM during the reionization epoch. Importantly, this approach requires an estimate of the intrinsic Ly $\alpha$  emission line in order to determine the contribution from the smooth component absorption of the IGM damping wing. Using this technique, limits on the IGM neutral fraction at  $z > 6$  have been obtained (e.g. Mesinger & Haiman 2007; Bolton et al. 2011; Schroeder et al. 2013).

In the absence of a viable method to recover the intrinsic Ly $\alpha$  emission profile, one can attempt to use an emission template constructed from a QSO composite spectrum. Numerous composite spectra exist, constructed by averaging over a vastly different number of QSOs (e.g. Francis et al. 1991; Brotherton et al. 2001; Vanden Berk et al. 2001; Telfer et al. 2002; Shull, Stevans & Danforth 2012; Stevans et al. 2014; Harris et al. 2016). However, by construction, these composite spectra only describe the average properties of QSOs, not the intrinsic variations of individual QSOs. Not accounting for these intrinsic properties can bias estimates of the IGM damping wing (Mortlock et al. 2011; Bosman & Becker 2015).

An alternative method is to reconstruct a template using a principle component analysis (PCA; e.g. Boroson & Green 1992; Francis et al. 1992; Suzuki et al. 2005; Suzuki 2006; Lee & Spergel 2011; Pâris et al. 2011). An improvement over the use of a composite spectrum, this approach aims to use the minimal subset of eigenvectors to characterize the QSO emission profile. For example, Francis et al. (1992) find that 3 eigenvectors are sufficient to describe 75 per cent of the observed profile variation and 95 per cent if 10 eigenvectors are used. Beyond 10, the eigenvectors obtain little information and become rather noisy (Suzuki et al. 2005). However, these eigenvectors are extracted from a fit to the original QSO spectrum. Therefore, given that the Ly $\alpha$  line cannot be directly recovered at high redshifts, in order to obtain an estimate of the intrinsic Ly $\alpha$  profile some form of reconstruction/extrapolation of the relevant eigenvectors that describe Ly $\alpha$  would be required.

Conveniently, studies of these QSO composites and PCA approaches have revealed a wealth of information regarding correlations amongst various emission lines and other observable properties of the source QSO. For example, the first eigenvector of Boroson & Green (1992) showed that in the H  $\beta$  region, a strong anticorrelation existed between [O III] and Fe II. Furthermore, Hewett & Wild (2010) performed an in-depth exploration to establish relationships between emission-line profiles and the source systemic redshift to reduce the scatter and biases in redshift determination. More directly relevant for this work, both Shang et al. (2007) and Kramer

& Haiman (2009) observe a strong correlation between the Ly $\alpha$  and C IV peak blueshifts.

Motivated by the existence of correlations amongst the various emission-line properties, and the lack of either a robust physical model of quasar emission regions (e.g. Baldwin et al. 1995) or a method to recover the intrinsic Ly $\alpha$  profile within high- $z$  or heavily Ly $\alpha$ -obscured QSOs, we propose a new method to reconstruct the intrinsic Ly $\alpha$  emission-line profile for any high- $z$  or Ly $\alpha$ -obscured QSO. In this work, we develop our reconstruction method using QSOs selected from the Baryon Oscillation Spectroscopic Survey (BOSS; Dawson et al. 2013), a component of SDSS-III (Eisenstein et al. 2011). In summary, our Ly $\alpha$  reconstruction method is as follows.

- (i) Perform a Monte Carlo Markov Chain (MCMC) fit to a subset of emission lines for each of our selected QSOs.
- (ii) Construct a covariance matrix that describes all correlations amongst the QSO emission lines.
- (iii) Assume a  $N$ -dimensional Gaussian likelihood function to describe the covariance matrix.
- (iv) MCMC fit a high- $z$  or Ly $\alpha$ -obscured QSO characterizing all lines except Ly $\alpha$ .
- (v) Use the recovered emission-line information from the QSO to statistically characterize the intrinsic Ly $\alpha$  line.

The remainder of this paper is organized as follows. In Section 2, we discuss the observational data used within this work and the selection criteria we apply to construct our sample of QSOs. In Section 3, we describe our MCMC fitting procedure and how we model the QSO continuum, emission-line features and other components to aid the estimation of the observed QSO flux. With all the data obtained from fitting our entire QSO sample, in Section 4, we construct our covariance matrix and discuss the major correlations and recovered features. In Section 5, we outline our Ly $\alpha$  reconstruction method and highlight the performance of this approach. Following this, in Section 6, we provide a discussion of the potential applications for both the MCMC fitting algorithm and the Ly $\alpha$  reconstruction pipeline. Finally, in Section 7, we finish with our closing remarks.

## 2 DATA

In this work, we select our QSOs from Data Release 12 (DR12; Alam et al. 2015) of the large-scale SDSS-III observational programme BOSS (Dawson et al. 2013). The full details of the SDSS telescope are available in Gunn et al. (2006) and the details of the upgraded SDSS/BOSS spectrographs may be obtained in Smee et al. (2013). For reference, the wavelength coverage of the BOSS spectrograph is  $3600 \text{ \AA} < \lambda < 10400 \text{ \AA}$  in the observed frame, with a resolution of  $R \sim 2000\text{--}2500$  corresponding to pixel resolution of  $\sim 120\text{--}150 \text{ km s}^{-1}$ . The QSO target selection for BOSS consisted of a variety of schemes, including colour and variability selection, counterparts to radio and X-ray sources and previously known QSOs (Bovy et al. 2011; Kirkpatrick et al. 2011; Ross et al. 2012). The candidate QSO spectra were then visually inspected following the procedure outlined in Pâris et al. (2016), with updated lists of confirmed QSOs for DR12 available online.<sup>1</sup> Furthermore, we use the publicly available flux calibration model of Margala et al. (2015) to perform the spectrophotometric corrections of the DR12 QSO fluxes.

<sup>1</sup> <http://www.sdss.org/dr12/algorithms/boss-dr12-quasar-catalog/>

In total, DR12 contains 294 512 uniquely identified QSOs, 158 917 of which are observed within the redshift range  $2.15 < z < 3.5$ . The principal science goal of the BOSS observational programme was the detection of the baryon acoustic oscillation scale from the Ly $\alpha$  forest. To perform this, only relatively low to moderate S/N QSOs are required (e.g. White 2003; McDonald & Eisenstein 2007). However, within this work, we aim to statistically characterize the correlations between numerous QSO emission lines that require much higher signal to noise (S/N).

To construct the QSO sample used within this work, we preferentially selected QSOs with a median S/N across all filters (*ugriz*) of  $S/N > 15$  ('snMedian > 15'). This choice is arbitrary and, in principle, we could go lower; however, for decreasing S/N, the weaker emission lines become more difficult to differentiate from the noise, reducing potential correlations. We selected QSOs containing broad-line emission using the 'BROADLINE' flag and removed all sources visually confirmed to contain broad absorption lines (BALs) by using the 'QSO' selection flag. Furthermore, only QSOs with 'ZWARNING' set to zero are retained, where the redshifts were recovered with high confidence from the BOSS pipeline. Finally, we restrict our QSO redshift range to  $2.08 < z < 2.5$ ,<sup>2</sup> selecting QSOs by their BOSS pipeline redshift<sup>3</sup> (e.g. Bolton et al. 2012; see Appendix A for a more in-depth discussion on our adopted choice of BOSS redshift). Following these selection cuts, we recover a total QSO sample of 3862.<sup>4</sup>

Though the total QSO number of 3862 appears small, it should be more than sufficient to elucidate any statistically significant correlations amongst the emission-line parameters.<sup>5</sup> Furthermore, to properly assess the MCMC fitting to be discussed in Section 3, a detailed visual inspection will be required, therefore it is preferential to restrict the sample size. In selecting our redshift range of  $2.08 < z < 2.5$ , we are assuming there is no strong variation in the emission-line profiles of QSOs across the age of the Universe. That is, the covariance matrix recovered from this QSO sample will always be representative of the underlying QSO population. In Becker et al. (2013), these authors constructed 26 QSO composite spectra in the range of rest frame  $1040 < \lambda < 1550 \text{ \AA}$  across the redshift range of  $2 < z < 5$ . They found for Ly $\alpha$  and the emission lines redward, no significant variation with redshift, lending confidence to our assumption.

Note that throughout this work, we do not deredden our QSOs to account for interstellar dust extinction within the Milky Way (e.g. Fitzpatrick 1999). The dust extinction curve varies strongly in the

UV and ultimately will impact the Ly $\alpha$  line more than the C IV line. However, this will not greatly impact our results as we are attempting to reconstruct the Ly $\alpha$  emission line using a covariance matrix of correlations from other emission lines. Applying the extinction curve will only impact slightly on the peak of the emission lines, not the other characteristics of the line profile. When highlighting the performance of the reconstruction process in Section 5, we see that this slight overestimate should be well within the errors of the reconstructed profile.

### 3 MCMC QSO FITTING

We now introduce our MCMC fitting procedure. In Section 3.1, we outline and justify the selection of the emission lines considered. In Section 3.2, we then detail the construction of the QSO template. In order to improve the ability to recover the intrinsic emission-line profile and QSO continuum, we outline the treatment of 'absorption' features in Section 3.3. In Section 3.4, the iterative MCMC fitting procedure is discussed and an example is presented. Finally, in Section 3.5, we perform a visual quality assessment of our entire sample of fit QSOs to remove contaminants that could impact the observed emission-line correlations.

#### 3.1 Emission-line selection

Owing to the limited wavelength coverage of BOSS, the selection of available emission lines to be used is limited. Due to the complexity in observing high- $z$  ( $z \gtrsim 6$ ) QSOs, where Ly $\alpha$  is redshifted into the near-infrared (IR), the emission lines we use from the BOSS sample needs to be consistent with what is detectable with near-IR instruments such as Keck/MOSFIRE (McLean et al. 2010, 2012) and VLT/X-Shooter (Vernet et al. 2011).

The strongest emission lines, especially Ly $\alpha$ , C IV and Mg II, are known to contain a broad and narrow component (e.g. Wills et al. 1993; Baldwin et al. 1996; Vanden Berk et al. 2001; Shang et al. 2007; Kramer & Haiman 2009; Shen et al. 2011). These different components are thought to arise from moving clouds of gas above and below the accretion disc known as the broad- and narrow-line regions. Note that for our purposes, the physical origins of these components is irrelevant; a double Gaussian merely provides us a flexible basis set in which to characterize the line profile. Throughout this work, we will approximate all emission lines to have a Gaussian profile. While emission-line profiles are known to be Lorentzian (e.g. Peebles 1993), the fitting of a Lorentzian profile is complicated by the requisite identification of the broader wings relative to the uncertainty in the QSO continuum.<sup>6</sup> Ultimately, this is a subtle difference as we are only interested in characterizing the total line profile.

In order to decide which strong emission-line profiles should be fit with a single or double component Gaussian,<sup>7</sup> we perform a simple test analysing the Bayes information criterion (BIC; Schwarz 1978;

<sup>2</sup> This choice of redshift range was a trade-off between the wavelength coverage of the spectrograph and requiring that we were sufficiently blueward of rest-frame Ly $\alpha$  to characterize the line profile (arbitrarily chosen to be 1180 Å, corresponding to  $\sim 3600 \text{ \AA}$  at  $z = 2.08$ ), while also including the Mg II emission line ( $\lambda = 2798.75 \text{ \AA}$ , corresponding to  $\lambda = 10\,000 \text{ \AA}$  at  $z = 2.5$ ).

<sup>3</sup> Note that the rms of the quasar redshift error distribution for the BOSS pipeline redshift from DR9 was determined to be  $550 \text{ km s}^{-1}$  with a mean offset of the quasar redshift (bias) of  $\sim -150 \text{ km s}^{-1}$  (Font-Ribera et al. 2013).

<sup>4</sup> We computed the absolute AB magnitude from the QSO continuum at  $1450 \text{ \AA}$  ( $M_{1450}$ ) for this sample of QSOs and recovered a median of  $M_{1450} = -26.1$  with an interquartile range of 0.7.

<sup>5</sup> The errors and biases when attempting to accurately measure the covariance matrix of a set of parameters ( $N_{\text{par}}$ ) from a total number of sources ( $N_{\text{src}}$ ) scales approximately as  $N_{\text{par}}/N_{\text{src}}$  (e.g. Dodelson & Schneider 2013; Taylor & Joachimi 2014; Petri, May & Haiman 2016). Within this work, we ultimately construct an 18 parameter covariance matrix from a subsample of 1673 QSOs, corresponding to an expected error of  $\sim 1$  per cent.

<sup>6</sup> In practice, thermal (or other) broadening will make the Lorentzian wings irrelevant in the case of active galactic nuclei (AGN) emission lines. For even the modest thermal broadening of  $\sim 10 \text{ km s}^{-1}$ , only the Gaussian core can be detected (see e.g. fig. 4 of Dijkstra 2014).

<sup>7</sup> In principle, we could allow for  $N > 2$  components to our line fitting procedure. For example, several authors have fitted three Gaussian components to the C IV emission-line profile (e.g. Dietrich et al. 2002; Shen et al. 2008, 2011). However, in this work, we attempt to avoid adding too much complexity to the fitting method.

Liddle 2004) of each of the individual line profiles in Appendix B. Below we summarize our findings.

(i)  $\text{Ly}\alpha$ : the strongest observed UV emission line. In order to better characterize the fit to the line profile, a two component Gaussian is preferred. This is well known and consistent with other works.

(ii)  $\text{Si IV} + \text{O IV}$ : this line complex consists of both the  $\text{Si IV}$  ( $\lambda 1396.76 \text{ \AA}$ ) and  $\text{O IV}$  ( $\lambda 1402.06 \text{ \AA}$ ) line centres. Unfortunately, these individual line profiles are intrinsically broad, preventing our ability to distinguish between them. Therefore, these two lines appear as a single, blended line. In Appendix B, we find a single Gaussian component is sufficient to characterize the line profile.

(iii)  $\text{C IV}$ : this line profile is a doublet ( $\lambda\lambda 1548.20, 1550.78 \text{ \AA}$ ). Again, both components being intrinsically broad prevents individual detection, therefore the line profile is observed as a single, strong line. For the  $\text{C IV}$  line, we find a two component Gaussian to be preferable to characterize the line.

(iv)  $\text{C III}$ : for the  $\text{C III}$  line ( $\lambda 1908.73 \text{ \AA}$ ), we find a single component Gaussian to be sufficient to characterize the line. For almost all of the BOSS QSOs in our sample, the nearby, weak  $\text{Si III}$  line ( $\lambda 1892.03 \text{ \AA}$ ), which would appear on top of the much broader  $\text{C III}$  line is not resolvable.<sup>8</sup> Furthermore, the  $\text{C III}$  line may also be contaminated by a continuum of low-ionization Fe lines, however, unlike  $\text{Mg II}$  (see next), the relative impact on the  $\text{C III}$  line is minor.

(v)  $\text{Mg II}$ : while the  $\text{Mg II}$  line ( $\lambda 2798.75 \text{ \AA}$ ) is observable within the wavelength range of our BOSS QSO sample, we choose not to fit this emission profile. This is because of the contamination from the Fe pseudo-continuum. Though Fe emission templates exist (e.g. Vestergaard & Wilkes 2001), the fitting procedure is complicated. One must simultaneously fit several spectral regions in order to calibrate the true flux level of the Fe pseudo-continuum in order to remove it and obtain an estimate of the  $\text{Mg II}$  emission line. Since we aim to simultaneously fit the full QSO spectrum, this approach would add degeneracies to the model (e.g. between the true continuum and the Fe pseudo-continuum). While this can be overcome, it requires first fitting the QSO continuum blueward of  $\text{Mg II}$ , before fitting the Fe pseudo-continuum, which reduces the flexibility of our model.

In addition to these lines above, we also consider several other lines all modelled by a single Gaussian. These include: (i)  $\text{N V}$  ( $\lambda\lambda 1238.8, 1242.8 \text{ \AA}$ ), which is an important line for characterizing the  $\text{Ly}\alpha$  line profile as it can be degenerate with the broad  $\text{Ly}\alpha$  line component, (ii)  $\text{Si II}$  ( $\lambda 1262.59 \text{ \AA}$ ), (iii) the  $\text{O I/Si II}$  blended

<sup>8</sup> In principle, by ignoring the  $\text{Si III}$  feature, the centroid of the measured  $\text{C III}$  line can be shifted bluer than its true value. Quantitatively, we determine the extent of this blueshift by fitting all QSOs within our sample that have a clear, discernible  $\text{Si III}$  feature. We find that by excluding  $\text{Si III}$ , the average recovered  $\text{C III}$  emission-line centre is blueshifted by  $\sim 310 \text{ km s}^{-1}$  (with the associated linewidth broadened by  $\sim 315 \text{ km s}^{-1}$ ). This sample, however, only contains 57 (out of 1673) QSOs, corresponding to only  $\sim 3.4$  per cent of the full ‘good’ sample affected by this blueshift. For the vast majority of QSOs in our sample, the  $S/N$  around  $\text{C III}$  is insufficient to tease out the individual emission component of the  $\text{Si III}$  feature. Therefore, owing to the small resultant blueshift in the line centre estimate (compared to the average dispersion of  $\sim 550 \text{ km s}^{-1}$  in the redshift estimate of the chosen BOSS pipeline redshift) and the corresponding low number of sources potentially affected by this systematic shift, we deem the exclusion of  $\text{Si III}$  a valid simplification. As a final point, owing to the weak total flux expected in the  $\text{Si III}$  emission line, including this in the MCMC fitting for the full QSO sample (where  $\text{Si III}$  is not clearly present) would cause a strong degeneracy with the  $\text{C III}$  line unless extremely strong priors on the line shape are imposed.

complex ( $\lambda 1304.35, \lambda 1306.82 \text{ \AA}$ ), (iv)  $\text{C II}$  ( $\lambda 1335.30 \text{ \AA}$ ), (v)  $\text{He II}$  ( $\lambda 1640.42 \text{ \AA}$ ), (vi)  $\text{O III}$  ( $\lambda 1663.48 \text{ \AA}$ ) and (vii)  $\text{Al III}$  ( $\lambda 1857.40 \text{ \AA}$ ).

### 3.2 Continuum and emission-line template

In this work, we fit the rest-frame wavelength range ( $1180 \text{ \AA} < \lambda < 2300 \text{ \AA}$ ) with a single power law for the QSO continuum,

$$f_\lambda = f_{1450} \left( \frac{\lambda}{1450 \text{ \AA}} \right)^{\alpha_\lambda} \text{ erg cm}^{-2} \text{ s}^{-1} \text{ \AA}^{-1}, \quad (1)$$

where  $\alpha_\lambda$  describes the spectral slope of the continuum and  $f_{1450}$  is the normalization of the QSO flux that we choose to measure at  $1450 \text{ \AA}$ . While we normalize the QSO flux at  $1450 \text{ \AA}$ , we allow this quantity to vary within our MCMC fitting algorithm (by adding a small, variable perturbation). While this quantity does not depart greatly from the original normalized value, it allows us to compensate for situations where the nearby region around  $1450 \text{ \AA}$  might be impacted by line absorption or a noise feature from the spectrograph.

Secondary (broken) power-law continua have been fit to QSO spectra at  $\lambda > 4500 \text{ \AA}$  for an independent red continuum slope (e.g. Vanden Berk et al. 2001; Shang et al. 2007); however, this is beyond our QSO sample wavelength coverage. Typically, a broken power-law continuum is also adopted blueward of  $\text{Ly}\alpha$ , visible in low- $z$  *Hubble Space Telescope* spectra (e.g. Telfer et al. 2002; Shull et al. 2012). In this work, we do not consider a different slope near  $\text{Ly}\alpha$  as we only fit down to  $1180 \text{ \AA}$ , therefore there is insufficient information to include a secondary component. By only considering a single power law through the  $\text{Ly}\alpha$  line profile, we may bias our results slightly on fitting the  $\text{Ly}\alpha$  broad component. However, provided we are consistent in our usage of this QSO continuum between this fitting approach and the reconstruction method, this should not impact our results.

As mentioned in the previous section, we model each emission-line component with a Gaussian profile. Following Kramer & Haiman (2009), the total flux for each component can be defined as

$$F_i = a_i \exp \left[ - \frac{(\lambda - \mu_i)^2}{2\sigma_i^2} \right], \quad (2)$$

where  $a_i$  describes the amplitude of the line peak,  $\mu_i$  is the location of the line centre in Armstrong,  $\sigma_i$  is the width of the line in Armstrong and the subscript ‘ $i$ ’ denotes the specific line species (e.g.  $\text{Ly}\alpha$ ). Note that within this work, the peak amplitude is always normalized by the continuum flux at  $1450 \text{ \AA}$ ,  $f_{1450}$ , therefore it is always a dimensionless quantity. More intuitively, the line centre location,  $\mu_i$ , can be written in terms of a velocity offset relative to the systemic line centre,

$$v_{\text{shift},i} = c \frac{\mu_i - \lambda_i}{\lambda_i} \text{ km s}^{-1}, \quad (3)$$

and the linewidth can be expressed as

$$\sigma_i = \lambda_i \left( \frac{\text{LW}}{c} \right) \text{ \AA}, \quad (4)$$

where LW is the linewidth measured in  $\text{km s}^{-1}$ . Throughout equations (2)–(4), both  $\lambda$  and  $\lambda_i$  are measured in the rest frame.

Each Gaussian line component can therefore be fully described by its three component parameters, the linewidth, peak amplitude and velocity offset. In total, we fit each QSO with two continuum parameters, two double component Gaussians ( $\text{Ly}\alpha$  and  $\text{C IV}$ ) and

nine single component Gaussian profiles, resulting in a total of 41 continuum and emission-line parameters.

### 3.3 Identifying absorption features

Intervening diffuse neutral hydrogen or larger column density absorbers (smaller than DLAs) along the line of sight can produce narrow absorption features. Furthermore, metal pollution in stronger absorption systems can additionally result in narrow absorption features appearing in the observed profiles of the emission lines.

These narrow features, if not measured and accounted for, can artificially bias the shape and peak amplitude of the emission-line components. Therefore, in this section, we outline our approach for identifying these features in a clean and automated manner:

- (i) Identify all flux pixels that are a local minima within a  $2 \text{ \AA}$  region surrounding the central pixel in question. This choice of  $2 \text{ \AA}$  is arbitrary, but is selected to be sufficiently broad to ignore features that might arise from noise fluctuations.
- (ii) Construct a horizontal line of constant flux that begins from the global flux minimum.
- (iii) Incrementally increase this line of constant flux, recording the depth and width of each absorption feature enclosed by the line of constant flux.
- (iv) If the depth becomes larger than  $3\sigma$  ( $5\sigma$  in the vicinity of  $\text{Ly}\alpha$ ) of the observed error in the flux at that pixel and the candidate absorption line has remained isolated (i.e. not overlapped with a nearby feature), it is then classified as an absorption line.

Our adopted choice of  $3\sigma$  ( $5\sigma$  near  $\text{Ly}\alpha$ ) arises after rigorously testing this pipeline against the absorption features that were visually identified, until the vast majority of the absorption lines could be robustly located by this procedure. Across the full QSO sample, we found a broad range in the number of features identified within each individual QSO, from only a few up to  $\sim 40$ . For each identified absorption feature, a single Gaussian (described by its own three parameters) is assigned and is simultaneously fit with the continuum and emission-line profiles outlined previously. Therefore, the total number of parameters to be fit per QSO varies.

### 3.4 MCMC sampling the QSO template

We fit each QSO within a Bayesian MCMC framework, using the  $\chi^2$  likelihood function to determine the maximum likelihood fit to the QSO spectrum. This choice enables us to fully characterize any potential model degeneracies between our model parameters, while also providing the individual probability distribution functions (PDFs) for each model parameter. In this work, we utilize the publicly available MCMC PYTHON code COSMOHAMMER (Akeret et al. 2013) built upon EMCEE (Foreman-Mackey et al. 2013) that is based on the affine invariant MCMC sampler (Goodman & Weare 2010).

Assuming flat priors across our  $>50$  model parameters and fitting the full high-resolution BOSS spectrum within the wavelength range ( $1180 \text{ \AA} < \lambda < 2300 \text{ \AA}$ ) simultaneously is computationally inefficient. Instead, we perform an iterative procedure to boost the computational efficiency that we outline below.

- (i) Normalize the full QSO spectrum at  $1450 \text{ \AA}$  and then fit the two continuum parameters,  $f_{1450}$  and  $\alpha_\lambda$  within a set of selected wavelength ranges of the full spectrum that are minimally contaminated by emission lines. We choose to fit the QSO continuum within

the regions [1275, 1295], [1315, 1330], [1351, 1362], [1452, 1520], [1680, 1735], [1786, 1834], [1970, 2040] and [2148, 2243]  $\text{\AA}$ .

- (ii) Break the full QSO spectrum up into wavelength regions centred around the emission lines. We choose [1180, 1350]  $\text{\AA}$  centred on  $\text{Ly}\alpha$ , [1350, 1450]  $\text{\AA}$  centred on  $\text{Si IV} + \text{O IV}$ , [1450, 1700]  $\text{\AA}$  centred on  $\text{C IV}$  and [1700, 1960]  $\text{\AA}$  centred on  $\text{C III}$ .

(iii) Within each of these four regions, we take the continuum estimated from above and then fit all emission lines and any absorption features that fall within the respective wavelength ranges. For each of these regions, we then perform an MCMC fit.

(iv) From the individual PDFs for each parameter, we construct a flat prior across a much narrower allowed range, driven by the width of the individual distributions from the fitting above.

(v) Finally, we fit the entire QSO spectrum using the entire model parameter set and recover a maximum likelihood model that describes the full spectrum.

In Fig. 1, we provide an example of one of the BOSS QSOs from our full sample. In this figure, we provide zoomed-in panels of both the QSO continuum (red dashed curve, top panel) and the various emission lines that are simultaneously fit within our MCMC approach across all other panels. This figure highlights that any notable absorption features have been identified by our pipeline and accurately characterized (e.g. the  $\text{Ly}\alpha$  line profile in the left-hand panel of the middle row). From Fig. 1, we note that this approach is able to fit the full spectrum. The maximum likelihood we obtained was  $\chi^2 = 3110$ , for which we had 2899 bins (from the raw spectrum) and 71 free parameters, corresponding to a reduced  $\chi^2$  of 1.1. For reference, this took  $\sim 1$  h on a single processing core, which can be rapidly improved if a binned spectrum is used.

### 3.5 QSO fitting quality assessment

After fitting the entire sample with our full MCMC QSO fitting pipeline, we are in a position to construct a higher fidelity sample of QSOs for constructing our covariance matrix and investigating the correlations amongst the emission-line parameters. This is performed by visually inspecting our QSO sample, applying a simple selection criteria. Following the completion of this selection process, we produce two separate QSO samples, one classified as ‘good’ and another classified as ‘conservative’, the details of which we discuss below (in Appendix C, we provide a few selected examples to visually highlight this subjective process). The criteria are outlined as follows.

- (i) We remove all QSOs with a poor characterization of the continuum. These include QSOs with a positive spectral index or a clear departure from a single power-law continuum. Only a handful of QSOs exhibit this behaviour. See Fig. C1 for some examples.

(ii) We further remove any QSOs that have either (i) missing sections of flux that overlap with any of the emission lines, (ii) a sufficient number of absorption features that cause a loss of confidence in the fitting of the  $\text{Ly}\alpha$  profile, (iii) either an intervening dense neutral absorber or sufficiently strong/broad absorption blueward of line centre that can impact the broad component of either the  $\text{Ly}\alpha$  or the  $\text{C IV}$  lines or (iv) an  $\text{Ly}\alpha$  line region that is not well fit or characterized by our double component Gaussian, which might arise from numerous absorption profiles or the lack of a prominent  $\text{Ly}\alpha$  peak.

(iii) Following the removal of these contaminants from our sample, we are left with 2653 QSOs, which we call our ‘conservative’

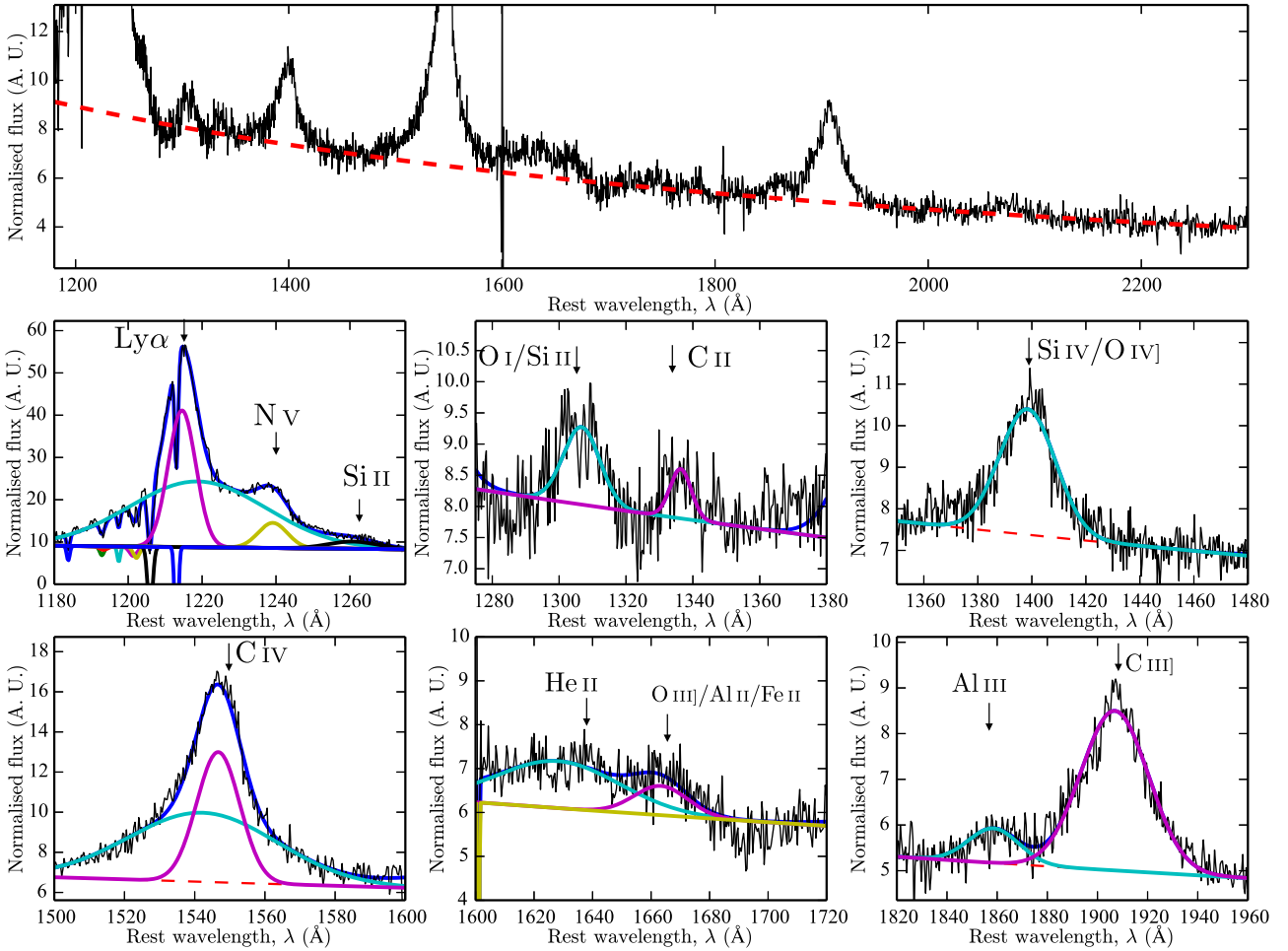


**Figure 1.** An example, zoomed-in figure of the MCMC QSO template fitting of a BOSS (SDSS-III) spectrum (‘spec-4185-55469-0076’ a  $z = 2.478$  QSO). For all spectra, we translate the flux into arbitrary units ( $1 \text{ au} = 10^{-17} \text{ erg cm}^{-2} \text{ s}^{-1} \text{ \AA}^{-1}$ ). Top: the full QSO spectrum used within our fitting procedure as a function of the rest-frame wavelength,  $\lambda$ . The red dashed curve corresponds to the two parameter continuum (see equation 1). Middle left: the two component fit to the Ly $\alpha$  emission profile highlighted by the broad (cyan) and narrow (magenta) components and a single Gaussian profiles for N v (yellow) and Si II (black). A series of ‘absorption’ features were identified and fit to the spectrum (shown below the continuum level). Middle centre: two low-ionization lines, O I (cyan) and C II (magenta). Middle right: single component fit to the Si IV + O IV] doublet. Bottom left: double component fit to C IV highlighted by the broad (cyan) and narrow (magenta) components. Bottom centre: Low-ionization lines, He II (cyan) and O III] (magenta). Bottom right: single component fit to C III] (magenta) and single Gaussian Al III component (cyan). The maximum likelihood fit to this spectrum was  $\chi^2 = 3110$ , for which we recovered a  $\chi^2_{\text{red}} = 1.1$  (with 2828 degrees of freedom, 2899 bins and 71 free parameters).

sample.<sup>9</sup> These can still include QSOs that might have absorption features centred on the Ly $\alpha$  line centre or absorption line complexes that might contaminate large sections of the Ly $\alpha$  line profile (see Fig. C3 for examples).

(iv) We then apply a secondary criteria, which preferentially selects QSOs which contain (i) fewer absorption features and (ii) no absorption features on the line centre. This results in a final sample of 1673 QSOs, which we refer to as our ‘good’ sample (see Fig. C4 for examples).

The major difference between the ‘good’ and ‘conservative’ sample is that the ‘conservative’ sample will contain QSO spectra for which we have less confidence in either the identification and

fitting of one or several of the emission lines due to the presence of absorption features. Ultimately, if we claim that any correlations amongst the emission lines are a universal property of the QSOs, then the covariance matrices of the two should be almost identical, with the ‘conservative’ sample containing additional scatter (slightly weaker correlations). In the next section, we construct our covariance matrices and investigate this further.

#### 4 DATA SAMPLE COVARIANCE

With the refined, quality-assessed QSO spectra from the previous section, we now construct our covariance matrix to characterize all correlations amongst the various emission lines.

##### 4.1 The covariance matrix

In performing the quality assessment of our QSO spectra, we note that a number of the weaker emission lines are not always well

<sup>9</sup> Our naming convention of ‘good’ and ‘conservative’ refers to the tightness of constraints recovered from the reconstruction procedure. The ‘conservative’ sample, with less assumptions on data quality, produces slightly broader errors relative to the ‘good’ sample.

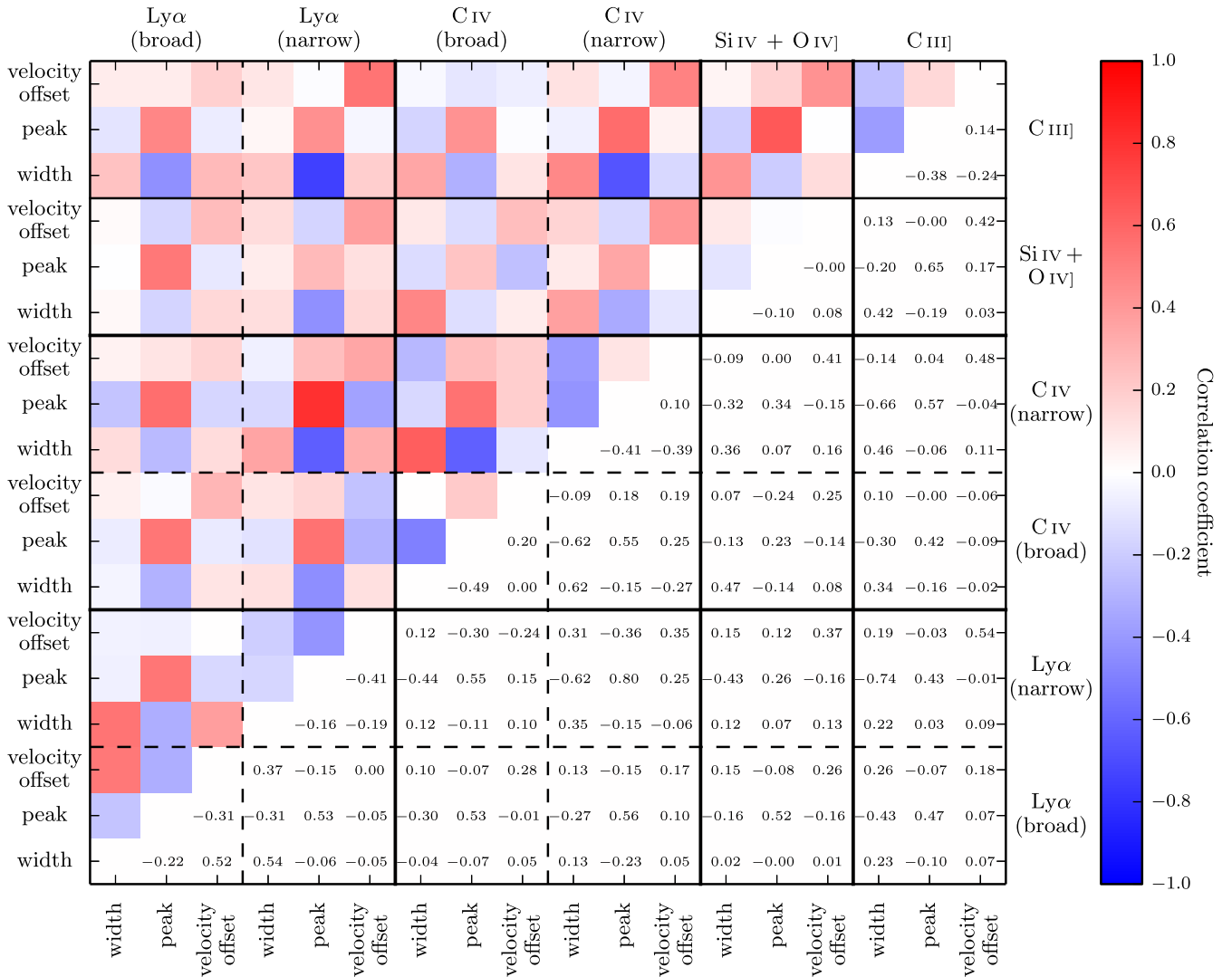


**Figure 2.** The correlation coefficient matrix (correlation coefficients listed in the lower half) constructed from the ‘good’ sample of 1673 QSOs. This  $18 \times 18$  matrix contains the double component Gaussians of Ly $\alpha$  and C IV and the single component Gaussians for Si IV + O IV] and C III]. Each Gaussian component contains three parameters, its peak width, peak height and velocity offset from systemic (Ly $\alpha$  + C IV + Si IV + O IV] + C III] =  $(2 \times 3) + (2 \times 3) + 3 + 3 = 18$  parameters).

characterized or resolved. This becomes more prevalent for the QSOs nearer to our sample limit of  $S/N = 15$ , which correspond to the highest density of QSOs in our sample. It would be interesting to investigate correlations between the strong high-ionization lines and the weaker low-ionization lines, as well as correlations amongst these two classifications. However, since these lines are not always readily available in our QSOs, we refrain from doing so. Regardless, by still attempting to fit these weaker lines, we retain the flexibility of the MCMC approach and, more importantly, this enables the QSO continuum to be estimated to a higher accuracy.

In light of this, we construct our covariance matrix from a subset of these emission lines: the most prominent emission lines that should always be resolvable in a lower  $S/N$  or lower resolution QSO spectrum (as in the near-IR for  $z > 6$  QSOs). The lines we identify are Ly $\alpha$ , Si IV + O IV], C IV and C III]. Since for Ly $\alpha$  and C IV we allow a broad and narrow component, we recover an  $18 \times 18$  covariance matrix. We choose to exclude the N v line from our covariance matrix for two reasons: (i) a clear, identifiable N v line is not always present in our QSO spectra, therefore including it would

artificially reduce any visible correlation and (ii) the ultimate goal of this work is the reconstruction of the Ly $\alpha$  line whereby including the N v line to the reconstruction process would only increase the complexity (the N v line should, in principle, be recoverable from the high- $z$  or Ly $\alpha$ -obscured QSO).

In Fig. 2, we present the correlation coefficient matrix that is obtained from the full covariance matrix from our ‘good’ sample of 1673 QSOs. In constructing this, we assume the standard format for the covariance matrix,  $\Sigma_{ij}$ , given by

$$\Sigma_{ij} = \frac{1}{N-1} \sum_i^N (\mathbf{X}_i - \boldsymbol{\mu}_i)(\mathbf{X}_j - \boldsymbol{\mu}_j), \quad (5)$$

where  $\mathbf{X}_i$  is the data vector for the full QSO sample and  $\boldsymbol{\mu}$  is the mean data vector for the  $i$ th parameter. For this data vector, we use the values from the parameter set that provide the maximum likelihood fit to each QSO. The correlation coefficient matrix,  $\mathbf{R}_{ij}$ ,

is then defined in the standard way,

$$\mathbf{R}_{ij} = \frac{C_{ij}}{\sqrt{C_{ii}C_{jj}}}, \quad (6)$$

where each diagonal entry,  $\mathbf{R}_{ij}$ , corresponds to the correlation coefficient between the  $i$ th and  $j$ th model parameters.

Note that for the covariance matrix, we do not include the two continuum parameters. First, for the parameters defining the emission-line peak, we define this parameter as the normalized peak value, where it is normalized by the continuum flux at  $f_{1450}$ . Therefore, if included, this would be completely degenerate with the peak amplitudes. Some correlation with continuum spectral index is expected, given that external (to the broad-line region) reddening will simultaneously weaken the bluer UV lines and redden the continuum spectral index. However, mild reddening is seen in only  $\sim 10$ – $20$  per cent of SDSS quasars (e.g. Richards et al. 2003; Hopkins et al. 2004) so this has little effect on the correlations (we find very weak correlations of the order of 10 per cent). Therefore, we do not report them, as these provide no additional information with respect to the individual line correlations.

#### 4.2 Interpreting the covariance matrix

In order to aid the interpretation of the correlation matrix, we divide Fig. 2 into the four emission-line species (denoted by black curves), while the narrow- and broad-line species are further separated by black dashed lines. Positive correlations are represented by a decreasing (weakening) shading of red, with white representing no correlation and an increasing blue scaling denotes a strengthening of the anticorrelation. Using the upper half of the correlation matrix enables a faster analysis of the correlation patterns amongst the emission-line parameters and the lower half reports the numerical value of the correlation (or anticorrelation). For the most part, each  $3 \times 3$  sub-matrix returns the same correlations and anticorrelations amongst the peaks, widths and velocity offsets, but with varying degrees of strength.

First, we note that with this correlation matrix, it is straightforward to note that all pairs of peak height parameters are positively correlated. This is to be expected as the peak amplitude is positively correlated with the QSO luminosity. This correlation between the peak heights is the strongest of the trends. Most importantly for this work, the correlations amongst the Ly $\alpha$  peak height parameters are the strongest. For example, we find the strongest correlation ( $\rho = 0.8$ ) between the peak height of the Ly $\alpha$  narrow component and the associated peak height of the C IV narrow component. In Fig. 3, we provide the two-dimensional scatter plot for this strong correlation (central panel) and the one-dimensional marginalized PDFs for the Ly $\alpha$  (top) and C IV (right). The green solid and dashed contours in the central panel denote the 68 and 95 per cent two-dimensional marginalized joint likelihood contours, which describe the relative scatter amongst our sample of QSOs. In the one-dimensional marginalized PDFs, the solid black curves are the histograms of the sample of QSOs, while the blue solid curves are an approximated one-dimensional Gaussian for that associated parameter. Note that in this figure, and in subsequent figures, these blue curves are not a fit directly to the raw data, rather instead they are approximations of a Gaussian PDF with  $1\sigma$  scatter equivalent to the raw data.

Returning to the correlation matrix, we additionally recover a relatively strong trend (anticorrelation) between the peak height and the linewidth. In Fig. 4, we provide the strongest of these anticorrelations ( $\rho = -0.74$ ) that is between the Ly $\alpha$  peak amplitude of the narrow-line component and the width of the single component C III]

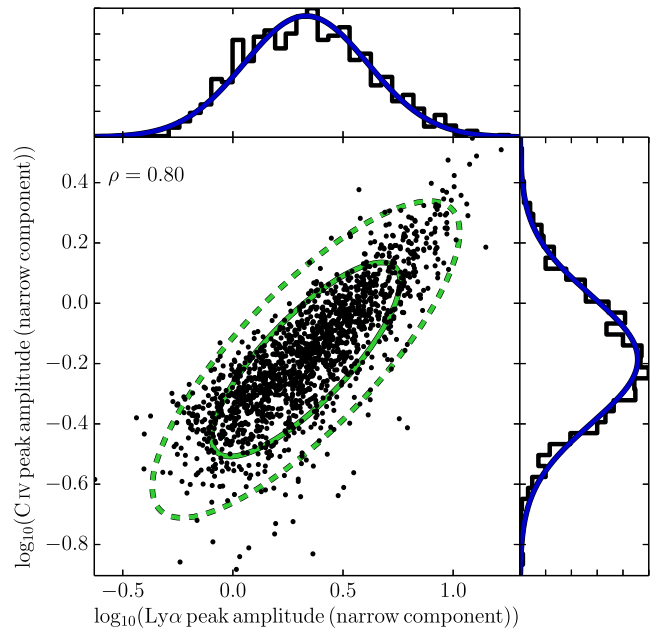


**Figure 3.** A two-dimensional scatter plot of the correlation between the peak amplitudes of the narrow components of the Ly $\alpha$  and C IV emission lines for our ‘good’ sample of 1673 QSOs. We recover a correlation coefficient of  $\rho = 0.80$ , indicative of a strong, positive correlation. The green solid and dashed curves correspond to the 68 and 95 per cent two-dimensional marginalized joint likelihood contours, respectively. The histograms (black curves) correspond to the recovered PDFs for each of the two parameters, while we also provide Gaussian curves (blue) representative of the scatter in the fit parameters (not a direct fit). Note that for the peak amplitude, we normalize by  $f_{1450}$ , therefore these are dimensionless.

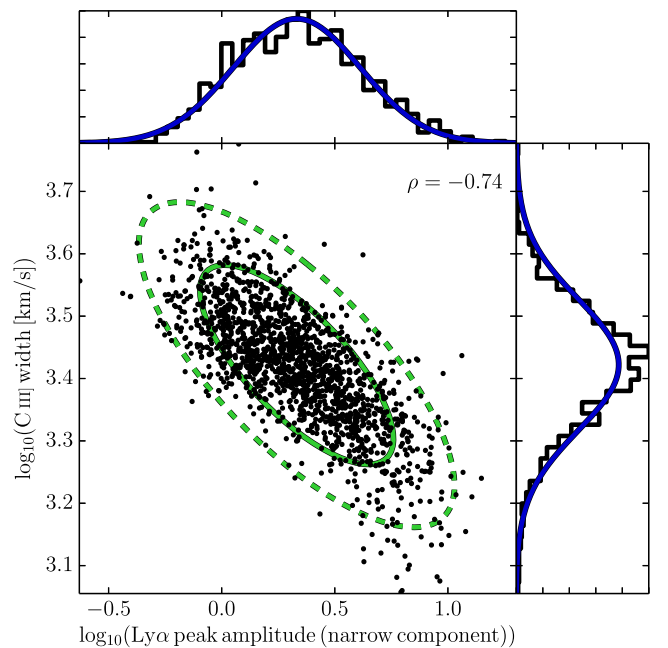


**Figure 4.** A two-dimensional scatter plot of the correlation between the narrow component of the Ly $\alpha$  peak amplitude and linewidth of the C III] emission line for our ‘good’ sample of 1673 QSOs. We recover a correlation coefficient of  $\rho = -0.74$ , indicative of a strong anticorrelation. Histograms, blue curves and the green contours are as described in Fig. 3. As in Fig. 3, the peak amplitude is normalized by  $f_{1450}$  and is therefore dimensionless.

line. We observe for an increasing peak amplitude for the Ly $\alpha$  narrow component, a decreasing of the C III] linewidth. This behaviour could be inferred as a result of the Baldwin effect (Baldwin 1977). For an increasing peak amplitude (i.e. QSO luminosity), we expect a weaker broad-line emission. Physically, a plausible scenario to describe this could be the overionization of the inner broad-line region by the continuum in high-luminosity QSOs, resulting in carbon being ionized into higher order species (i.e. no C IV/C III]). For these high-luminosity QSOs, the high-ionization lines may then predominantly arise at larger radii where the velocity dispersion is lower, producing smaller linewidths (e.g. Richards et al. 2011). Alternately, it could arise from systematics from our line fitting. As a result of the decreasing equivalent widths with increasing QSO luminosity, it could be that the single component Gaussian for the C III] does not characterize the line profile as accurately. With a less prominent broad-line component, the emission from the wings could be underestimated, producing a narrower C III] line.

We additionally recover a trend for a positive correlation between the widths of the various line species, though this is a relatively weaker trend. However, for the broad and narrow components for the same line species, we find more moderate correlations ( $\rho = 0.54$  for Ly $\alpha$  and  $\rho = 0.62$  for C IV). It is difficult to interpret these correlations though, as these broad and narrow lines are simultaneously fit and therefore, in principle, could be degenerate.

Shang et al. (2007) investigated correlations amongst the Ly $\alpha$ , C IV and C III] lines for a significantly smaller sample of 22 QSOs. These authors recover moderate to strong correlations between a few of their emission linewidth full width at half maxima (FWHMs). They find Ly $\alpha$ -C IV ( $\rho = 0.81$ ) and C IV-C III] ( $\rho = 0.53$ ). If we equate this FWHM as the width of the narrow component of our emission-line profiles, we find correlations between the same species of Ly $\alpha$ -C IV ( $\rho = 0.35$ ) and C IV-C III] ( $\rho = 0.46$ ).<sup>10</sup> While we recover an equivalent correlation for the C IV-C III] lines, we find a significant discrepancy for the Ly $\alpha$ -C IV lines. This potentially can be explained as an artificially large correlation owing to their small number of objects (22 compared to our 1683 QSOs).<sup>11</sup> Supporting this hypothesis, in Corbin & Boroson (1996) for a larger sample of 44 QSOs, this is reduced to  $\rho = 0.68$  for Ly $\alpha$ -C IV.

Additionally, Kramer & Haiman (2009) recovered a moderate positive correlation ( $\rho = 0.68$ ) between the velocity offsets for the Ly $\alpha$ -C IV components. For the same combination, Shang et al. (2007) found a stronger correlation of  $\rho = 0.81$ . In Fig. 5, we provide our weaker results between the narrow components of the Ly $\alpha$ -C IV lines for which we recover a moderate correlation of  $\rho = 0.35$ . Once again, this lack of an equivalently strong correlation in our sample could arise purely from the fact that our sample contains two orders of magnitude more QSOs. Shang et al. (2007) equivalently quote correlations of  $\rho = 0.45$  (Ly $\alpha$ -C III]) and  $\rho = 0.39$  (C IV-C III]). Using the narrow lines for Ly $\alpha$  and C IV, we find similarly moderate, but slightly stronger correlations of  $\rho = 0.54$  (Ly $\alpha$ -C III]) and  $\rho = 0.48$  (C IV-C III]).

In the construction of the covariance matrix and associated correlation matrix, we have only used the maximum likelihood val-

<sup>10</sup> By converting our fitted emission-line parameters (both broad and narrow) into a line profile FWHM width, we find correlations similar in strength to those recovered purely from the narrow-line component.

<sup>11</sup> Note that if we adopt a systemic redshift measured purely from a single ionization line (such as the Mg II redshift) rather than the pipeline redshift used throughout this work, we can recover a significantly stronger correlation of Ly $\alpha$ -C IV ( $\rho = 0.7$ ).

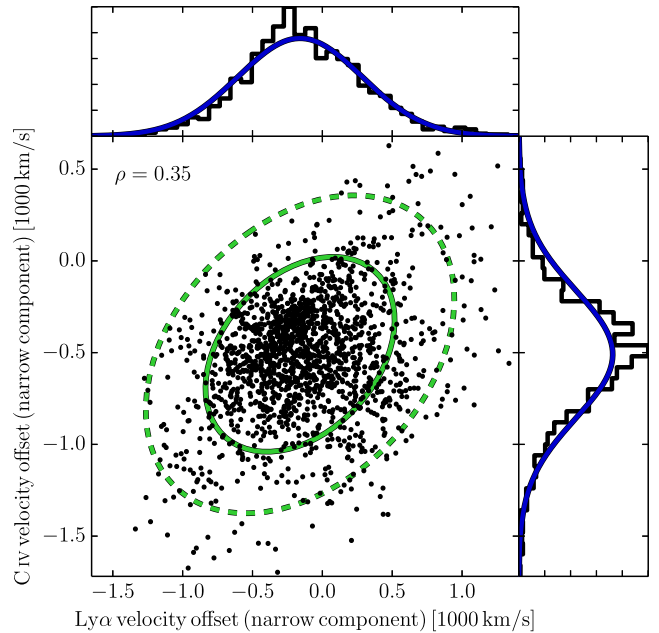


**Figure 5.** A two-dimensional scatter plot of the correlation between the velocity offsets of the Ly $\alpha$  and C IV emission lines for our ‘good’ sample of 1673 QSOs. We recover a correlation coefficient of  $\rho = 0.35$ , indicative of a moderate correlation, which is counter to the much stronger correlation hinted at from the smaller QSO samples of Shang et al. (2007) and Kramer & Haiman (2009). Histograms, blue curves and the green contours are as described in Fig. 3.

ues and ignored the relative errors for each parameter from the marginalized one-dimensional PDFs. Our reasoning for this is that the amplitude of the error on the individual parameters is small with respect to the scatter that arises for each parameter across the full QSO sample. In principle, however, we could perform an MCMC sampling of the full covariance matrix, allowing the means and all correlation coefficients to be free parameters. This would allow a more accurate characterization of both the individual errors for each parameter and the total scatter across the full QSO sample, potentially tightening the correlations amongst the emission-line parameters. However, this would require fitting  $\frac{1}{2}N(N+1)$  parameters encompassing both the means of the individual parameters and all correlation coefficients (in our case, 171 free parameters).

### 4.3 Correlation of the QSO continuum parameters

Though the continuum parameters are not included in the covariance matrix in Fig. 2, in Fig. 6, we provide the two-dimensional scatter between these two parameters. In our ‘good’ sample of QSOs, we recover only a relatively weak anticorrelation ( $\rho = -0.22$ ) between the QSO continuum spectral index,  $\alpha_\lambda$  and the normalization at 1450 Å ( $f_{1450}$ ). This weak anticorrelation likely arises due to dust reddening, which causes a drop in the normalization,  $f_{1450}$  and shallower spectral slopes. While both of these QSO parameters are well characterized by a Gaussian, the respective scatter in each parameter is considerable.

For our sample of ‘good’ (‘conservative’) QSOs, we recover a median QSO spectral index of  $\alpha_\lambda = -1.30 \pm 0.37$  ( $-1.28 \pm 0.38$ ). In contrast, Harris et al. (2016) construct a QSO composite spectrum with a wavelength coverage of ( $800 \text{ \AA} < \lambda < 3300 \text{ \AA}$ ) from the same BOSS DR12 sample. Using  $\sim 100\,000$  QSOs, these authors find a median spectral index for their QSO sample of  $\alpha_\lambda = -1.46$ ,

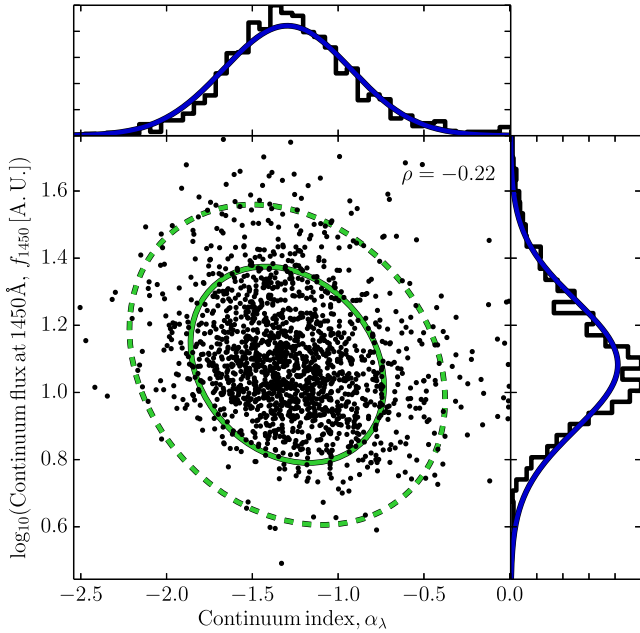


**Figure 6.** A two-dimensional scatter plot highlighting the correlation between the two QSO continuum parameters: the continuum spectral index,  $\alpha_\lambda$  and the continuum flux at 1450 Å,  $f_{1450}$  (for which we define 1 au =  $10^{-17}$  erg cm $^{-2}$  s $^{-1}$  Å $^{-1}$ ), for our sample of 1673 QSOs (the ‘good’ sample). We recover a correlation coefficient of  $\rho = -0.22$ , indicative of a weak anticorrelation. Histograms, blue curves and the green contours are as described in Fig. 3.

consistent with our results within the large scatter. However, these authors only fit the QSO continuum between 1440–1480 Å and 2160–2230 Å. Not fitting to the same spectral region likely results in a different recovered spectral slope. Furthermore, our estimate of  $\alpha_\lambda = -1.30$  ( $\alpha_\nu = -0.70$ ) is also consistent with the lower redshift samples of Scott et al. (2004) ( $\alpha_\nu = -0.56^{+0.38}_{-0.28}$ ), Shull et al. (2012) ( $\alpha_\nu = -0.68 \pm 0.14$ ) and Stevans et al. (2014) ( $\alpha_\nu = -0.83 \pm 0.09$ ). Note that within all these works, considerable scatter in the spectral index is also prevalent.

#### 4.4 Potential sample bias

In Sections 4.1 and 4.2, we presented the correlation matrix and discussions on the relative trends between the emission lines and their relative strengths. However, these results were drawn from our refined, quality assessed ‘good’ QSO sample. In order to guard against a potential bias that may have arisen following our specific selection process, we additionally construct the correlation matrix for our ‘conservative’ QSO sample. This ‘conservative’ sample contains ~1000 additional QSOs that are defined to be less robust than required for our ‘good’ sample. Therefore, this ‘conservative’ sample should contain more scatter amongst the recovered parameters, which would notably degrade the strength of the correlations relative to the ‘good’ sample if we have artificially biased our results.

In Fig. 7, we provide the matrix of the relative difference in the correlation coefficients between the ‘good’ and ‘conservative’ QSO samples. Here, we show the amplitude of the change in correlation coefficient between the two QSO samples. A positive (red) difference is indicative of the ‘good’ sample having a stronger correlation (either positive or anticorrelation), while a negative (blue) difference is indicative of the ‘conservative’ sample having a stronger correlation. Note that squares marked with a dot-dashed

cross indicate a change between a positive and anticorrelation, which arises when the correlations are close to zero in either sample.

For the most part, the relative change in the correlation is minor, of the order of  $|\Delta\rho| < 0.04$ . More importantly, for any of the strong correlations and notable trends we discussed in the previous section, we observe no sizeable differences, with the ‘good’ sample providing on average slightly stronger correlations (as indicated by the prevalence of red squares). For example, the Ly $\alpha$ –C IV peak heights of the narrow component from our ‘good’ sample was  $\rho = 0.80$ , whereas for the ‘conservative sample, it is  $\rho = 0.79$ . Therefore, in the absence of any drastic differences in the strong and notable trends discussed previously between the two samples, it is clear that we have not biased our QSO covariance matrix in the construction of the ‘good’ sample. Given that the relative amplitude of these differences between the two QSO samples is small and tends to be slightly weaker for the ‘conservative’ sample, the reconstructed profile recovered from the covariance matrix should recover effectively the same best-fitting Ly $\alpha$  profile, with slightly broader errors owing to the increased scatter (reduced correlations).

Equally, to be prudent, we considered several other ways to divide our QSO sample. First, we performed the same analysis, comparing instead the ‘conservative’ minus ‘good’ sample (the ~1000 QSOs from the ‘conservative’ sample not classified as ‘good’) and secondly, constructing two equally sized random samples from the ‘conservative’ sample. In both instances, we find the same strong correlations as in Fig. 2 with similar amplitude variations between the respective correlation matrices as shown in Fig. 7.

Finally, our results on line parameter correlations are sensitive to the choice of redshift estimate and any inherent biases in those estimates. We discuss this issue in detail in Appendix A, but, in summary, we find that while different redshift estimates do result in slightly different covariance matrices, our general conclusions are robust and the redshift estimate we have chosen (the BOSS pipeline redshift,  $z_{\text{pipeline}}$ ) performs the best at the Ly $\alpha$  profile reconstruction (see the next section).

## 5 LY $\alpha$ RECONSTRUCTION

We now use this covariance matrix to reconstruct the Ly $\alpha$  line profile. In this section, we outline the reconstruction pipeline and associated assumptions followed by an example of this approach.

### 5.1 Reconstruction method

Within our reconstruction approach, we approximate the distribution of the emission-line parameters (across the entire data sample) as a Gaussian.<sup>12</sup> In Figs 3–5, we observe that for these six parameters shown, this approximation is well motivated. Clearly, showing the 18 individual one-dimensional PDFs for each parameters would be uninformative, however, we confirm by eye that this approximation is valid for all model parameters. Note that in some of these cases, a Gaussian approximation holds only after taking the logarithm, especially for the normalized peak amplitude (normalized by  $f_{1450}$ ) and the emission linewidth. Importantly, if anything, these Gaussian approximations have a tendency to slightly overestimate

<sup>12</sup> The choice in adopting a Gaussian covariance matrix is driven by the large computational burden required to perform a full end-to-end Bayesian approach folding in all modelling uncertainties.

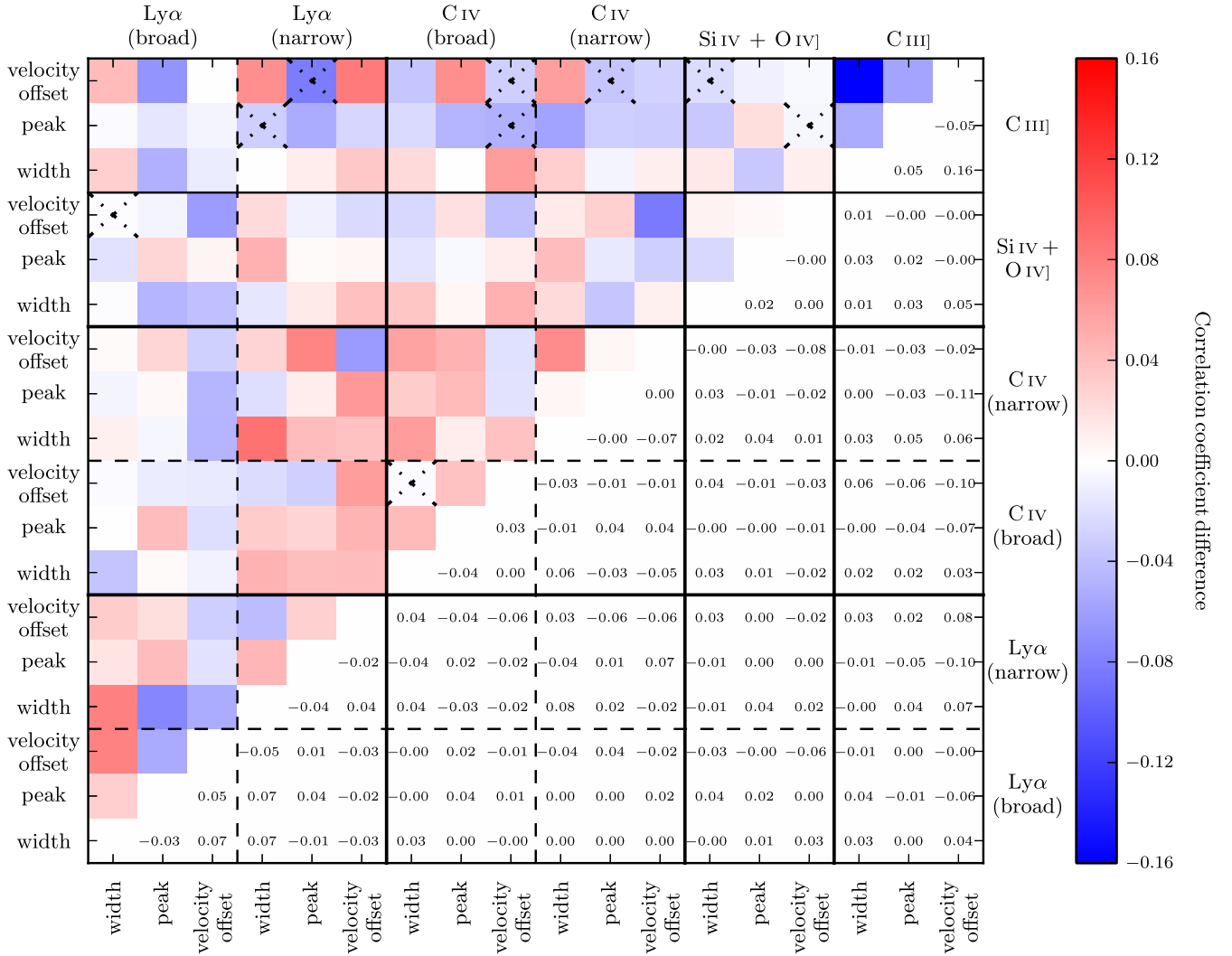


**Figure 7.** The amplitude of the difference of the correlation coefficients for the  $18 \times 18$  covariance matrix between the ‘good’ (1673) and ‘conservative’ (2653) QSO data sets. Positive (red) differences indicate where the correlation in the ‘good’ sample is greater than the ‘conservative’ and negative (blue) indicates when the ‘conservative’ sample is strongest. Note that this does not differentiate between a positive or anticorrelation nor the strength of the original correlation, just a strengthening/weakening of the respective correlation. Dot-dashed squares indicate a swap between a positive and negative correlation (typically indicative of the correlation coefficients in either QSO samples being close to zero). The colour bar has been renormalized relative to Fig. 2 to indicate the strength of the difference in amplitude.

the relative scatter within each parameter (see Fig. 5 for example), therefore this assumption in fact turns out to be a conservative estimate of the true scatter. The Gaussian nature of the scatter in Figs 3–5 and the conservative overestimation of the errors by our Gaussian approach lends confidence that our approach should not significantly underestimate the errors that one might recover from a fully Bayesian approach.

In order to perform the reconstruction, we assume that the QSO can be fit following the same procedure outlined in Section 3, except now we only fit the QSO redward of  $1275 \text{ \AA}$ . Our choice of  $\lambda > 1275 \text{ \AA}$  is conservatively selected to be both close enough to Ly $\alpha$  as possible, but with minimal to no contamination from emission-line wings, namely Ly $\alpha$ , N V or Si II. Furthermore, given that this approach is best suited for recovering the intrinsic Ly $\alpha$  profile from an Ly $\alpha$ -obscured or high- $z$  QSO, it is best to be sufficiently far from any possible contamination of the Ly $\alpha$  line region.

We can then define the  $N$ -dimensional parameter space (i.e. our 18 emission-line parameters outlined previously) as an  $N$ -dimensional

likelihood distribution given by

$$\mathcal{L} = \frac{1}{(2\pi)^{N/2} |\Sigma|} \exp \left[ -\frac{1}{2} (\mathbf{x} - \boldsymbol{\mu})^T \Sigma^{-1} (\mathbf{x} - \boldsymbol{\mu}) \right]. \quad (7)$$

Here,  $\Sigma$  is the recovered QSO covariance matrix (Section 4.1),  $\boldsymbol{\mu}$  is the data vector of the means obtained from the full QSO sample for each of the individual line profile parameters and  $\mathbf{x}$  is the data vector measured from our MCMC fitting algorithm for the individual obscured QSO spectrum.

After the Ly $\alpha$ -obscured or high- $z$  QSO has been fit following our fitting procedure, the recovered best-fitting values for the unobscured emission-line parameters are folded into equation (7). That is, we recover the best-fitting estimates of the Si IV + O IV], C IV and C III] emission lines and evaluate equation (7) to collapse the 18-dimensional likelihood function into a simple, six-dimensional likelihood function describing the six unknown Ly $\alpha$  emission-line parameters (two Gaussian components each defined by three parameters). The maximum likelihood of this six-dimensional

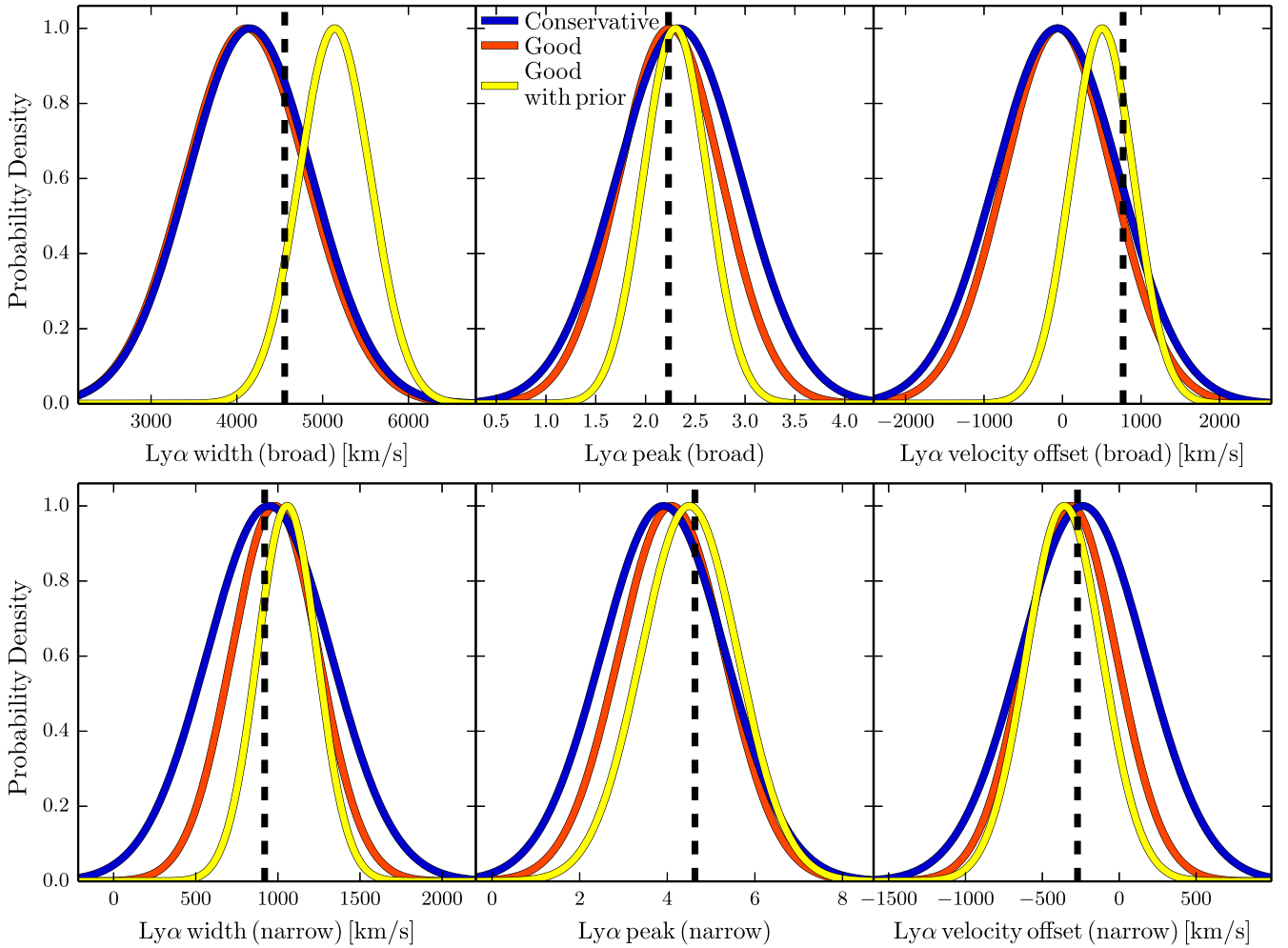


**Figure 8.** The recovered one-dimensional marginalized PDFs for each of the six reconstructed Ly $\alpha$  emission-line parameters obtained after applying the reconstruction method outlined in Section 5.1 to the example QSO in Fig. 1. The vertical dashed lines correspond to the MCMC maximum likelihood fit to the full QSO spectrum, whereas the blue and red curves correspond to the recovered one-dimensional PDFs obtained from using the covariance matrix constructed from the ‘conservative’ and ‘good’ QSO samples, respectively. The yellow curve corresponds to reconstructing the Ly $\alpha$  profile parameters using the ‘good’ sample while, in addition, applying a prior on the QSO flux within the range  $1230 < \lambda < 1275 \text{ \AA}$  (see Section 5.3 for further details). That is, we enforce our reconstructed Ly $\alpha$  emission-line profile to fit the observed spectrum within this region. Note that the peak amplitude is normalized by  $f_{1450}$  and is therefore dimensionless. Importantly, we are interested in the joint probability, i.e. the full Ly $\alpha$  line profile. As shown below, the reconstruction performs considerably better than can be inferred from these marginalized PDFs.

function then describes the best-fitting reconstructed profile for the Ly $\alpha$  emission line, while the full six dimensional matrix contains the correlated uncertainty.

## 5.2 Reconstruction example

We now present an example to highlight the performance of our approach. In order to do this, we choose the same QSO we showed in Fig. 1, fitting for  $\lambda > 1275 \text{ \AA}$  and recovering the six-dimensional estimate for the Ly $\alpha$  line profile. In restricting our fitting algorithm to  $\lambda > 1275 \text{ \AA}$ , we are not accessing all the information that was used by the full fit to estimate the QSO continuum. While this does not affect the recovery of the Ly $\alpha$  peak profile itself, the Ly $\alpha$  profile plus continuum could be affected. In Appendix D, we test this assumption, finding that the QSO continuum parameters can be recovered equivalently from these two approaches, with a small amount of scatter in the QSO spectral index.

Before providing the full reconstructed profile, we first recover the individual marginalized one-dimensional PDFs for each of the six Ly $\alpha$  emission-line parameters to better visualize the relative size of the errors. In order to obtain the recovered one-dimensional PDFs for the Ly $\alpha$  profile parameters, we marginalize the six-dimensional likelihood function over the remaining five Ly $\alpha$  parameters. In Fig. 8, we present these recovered one-dimensional marginalized PDFs, showing in the top row the Ly $\alpha$  broad-line component and in the bottom row the narrow-line component. The vertical black dashed lines represent the recovered values from fitting the full QSO in Fig. 1 and the coloured curves represent the recovered one-dimensional marginalized PDFs for each Ly $\alpha$  parameter for the ‘good’ sample (red) and ‘conservative’ sample (blue). It is clear that both QSO samples recover almost identical best-fitting values for each Ly $\alpha$  parameter, highlighting that both samples are characterized by the same correlations within the covariance matrix. Furthermore, the choice in constructing a ‘good’ sample is more evident here as consistently the ‘good’ sample provides marginally

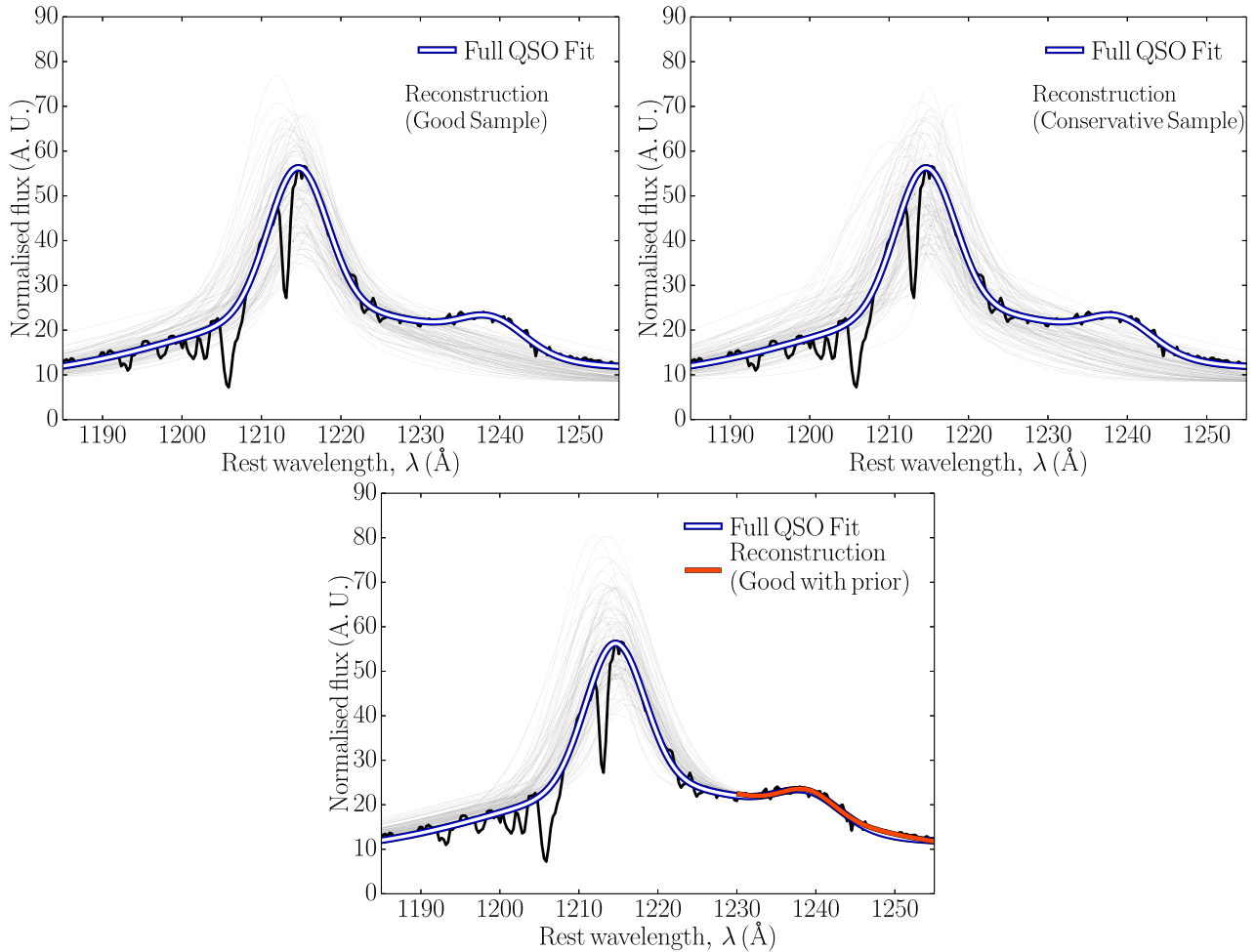


**Figure 9.** A zoom in of the recovered Ly $\alpha$  emission-line profile from our reconstruction procedure. The thin grey curves denote 100 Ly $\alpha$  line profiles extracted from the reconstructed six-dimensional Ly $\alpha$  likelihood function. These curves are randomly selected to represent the full posterior distribution for the reconstructed Ly $\alpha$  profiles, highlighting the relative scale of the errors. The white curves represent the original full MCMC fit of the same QSO (see Fig. 1). Black curves are the observed flux of the original QSO spectrum. Note that in these figures, we provide only the emission-line component of the full fit (i.e. absorption features are identified and fit, but not shown in the figure). Top left: the reconstructed profile from the ‘good’ sample. Top right: the reconstructed profile from the ‘conservative’ sample. Note that in both the top left and top right panels, the N v emission feature is not fit in the reconstruction procedure. Bottom: the reconstructed profile from the ‘good’ sample utilizing the flux prior applied within the range  $1230 < \lambda < 1275 \text{ \AA}$  (see Section 5.3 for further details).

narrower constraints. For the most part, the six reconstructed Ly $\alpha$  parameters are recovered within the 68 percentile limits of the original fit to the QSO, with the exception being the velocity offset of the broad Ly $\alpha$  component that is only slightly beyond this limit. Otherwise, the five remaining Ly $\alpha$  parameters are effectively centred around the expected value from the full fit to the same QSO (Fig. 1) that should enable a relatively robust recovery of the full Ly $\alpha$  line profile.

In Fig. 9, we provide the full reconstructed Ly $\alpha$  line profile. In the top left panel, we show the reconstructed Ly $\alpha$  line profile obtained from the ‘good’ QSO sample, whereas in the top right panel is the reconstructed profile from the ‘conservative QSO’ sample. In all figures, we present 100 reconstructed Ly $\alpha$  profiles denoted by the thin grey curves that are randomly drawn from the full posterior distribution. This small subset of reconstructed profiles highlight the relative scale of the variations in the total Ly $\alpha$  line profile peak height, width and position. The black curve is the raw data from the observed QSO, whereas the white

curve is the original fit to the full QSO spectrum as shown in Fig. 1.

In both, we find the total shape of the reconstructed Ly $\alpha$  line profile to match extremely well with the original full fit to the same QSO, highlighting the strength and utility of this covariance matrix reconstruction method. Both the ‘good’ and ‘conservative’ samples recover almost the identical reconstructed profile, though the ‘conservative’ QSO sample provides slightly broader errors. Note that for both these QSO samples, the reconstructed Ly $\alpha$  line profile is systematically below the original fit to the same QSO, indicated by the original QSO fit (white curve) being above the highest density of line profiles.<sup>13</sup> However, this systematic offset is only minor (less than 10 per cent in the normalized flux), well within the errors of the reconstruction. Referring back to Fig. 8, we can

<sup>13</sup> This is more prevalent when averaging over the full distribution of reconstructed Ly $\alpha$  profiles.

see that this underestimation appears due to the narrow component of the Ly $\alpha$  peak amplitude (bottom, central panel).

### 5.3 Improving the reconstruction with priors

We presented in Fig. 9 our best-fitting reconstructed Ly $\alpha$  profiles to a representative QSO drawn from our full sample. However, note that in this reconstruction method, we have only used information from the QSO spectrum above  $\lambda > 1275 \text{ \AA}$ . In doing this, for the case of our example QSO, we found our maximum likelihood estimates to slightly underestimate (by less than 10 per cent) the original Ly $\alpha$  line profile. At the same time, the total 68 per cent marginalized likelihoods of the reconstructed profiles are relatively broad. Motivated by this, we investigate whether we can provide an additional prior on the Ly $\alpha$  reconstruction profile to further improve the robustness of the recovered profile and to reduce the relative scatter.

In the top panels of Fig. 9, redward of Ly $\alpha$ , we see that the reconstructed Ly $\alpha$  line profile drops well below the observed flux of the original QSO. Given we are only reconstructing the Ly $\alpha$  line, this is to be expected as we are not recovering or fitting the N v emission line. However, in both Ly $\alpha$  obscured and high- $z$  QSOs, the N v emission line should be relatively unobscured, therefore the observed flux within this region could be used as a relative prior on the overall Ly $\alpha$  flux amplitude.

We therefore include a flux prior<sup>14</sup> into our Ly $\alpha$  reconstruction by performing the following steps.

(i) As before, we fit the QSO at  $\lambda > 1275 \text{ \AA}$ , recovering the QSO continuum and all emission-line profiles necessary for our covariance matrix approach.

(ii) Using these estimates, we collapse the 18-dimensional covariance matrix into a six-dimensional estimate of the intrinsic Ly $\alpha$  emission-line profile.

(iii) We then jointly MCMC sample the observed QSO spectrum within the range  $1230 < \lambda < 1275 \text{ \AA}$ . We fit the N v and Si II lines at the same time sampling from our six-dimensional reconstructed Ly $\alpha$  likelihood function obtained from the  $\lambda > 1275 \text{ \AA}$  fit. Fitting to the observed QSO flux and using the observed noise in the spectrum, we obtain a maximum likelihood for the reconstructed profile. In other words, we require the reconstructed Ly $\alpha$  line profiles to fit the observed spectrum over the range  $1230 < \lambda < 1275 \text{ \AA}$ .

Implementing this prior on the observed flux closer to  $\lambda = 1230 \text{ \AA}$ <sup>15</sup> accesses additional information on the Ly $\alpha$  profile that was not available through our original  $\lambda > 1275 \text{ \AA}$  reconstruction method. Near  $\lambda = 1230 \text{ \AA}$ , there should be a contribution from the Ly $\alpha$  broad-line component, which is somewhat degenerate with the N v line (as can be seen in Fig. 1). By simultaneously fitting the N v line and the Ly $\alpha$  likelihood function, we use this additional information to place a prior on the Ly $\alpha$  broad-line component, which should then reduce the overall scatter in the six-dimensional Ly $\alpha$  likelihood function.

<sup>14</sup> Note that this choice in phrasing does not imply a ‘prior’ in the Bayesian statistical sense, rather it is used to highlight that we are including additional information into our reconstruction procedure compared to the reconstruction method discussed in Section 5.1.

<sup>15</sup> This choice of  $1230 \text{ \AA}$  is purely arbitrary and is chosen based on the assumption that a damped absorption signal would not extend this far redward of Ly $\alpha$ . However, this choice is flexible and can be adjusted on a case-by-case basis if evidence for stronger attenuation beyond  $1230 \text{ \AA}$  is present.

Referring back to Fig. 8, we provide an example of this prior applied to the same QSO fit and reconstructed previously. In Fig. 8, the yellow curves represent the recovered one-dimensional marginalized PDFs for each of the six Ly $\alpha$  emission-line parameters. Immediately, it is clear that the application of this prior further reduces the relative error in the recovered PDFs. Furthermore, these PDFs remain centred on the originally recovered values, highlighting that we have not biased our reconstruction method.

In the bottom panel of Fig. 9, we present the full reconstructed Ly $\alpha$  profile after the addition of this prior. The red curve indicates the fit to the QSO within  $1230 < \lambda < 1275 \text{ \AA}$ , which we have used as our prior to improve the reconstruction of the Ly $\alpha$  line profile. At  $\lambda < 1230 \text{ \AA}$ , we then have the same 100 thin grey curves representing the full posterior distribution of the reconstructed Ly $\alpha$  likelihood profiles. By applying this additional prior on the total observed flux, we reduce the overall scatter in the reconstructed profile. The maximum likelihood profiles (thin grey curves) now provide a more robust match to the observed QSO.

### 5.4 Statistical performance of the reconstruction pipeline

Thus far, we have only applied our reconstruction pipeline to recover the Ly $\alpha$  line profile from a single, test example selectively drawn from our ‘good’ sample of 1673 QSOs. In order to statistically characterize the performance of the Ly $\alpha$  reconstruction pipeline across the QSO sample, in Fig. 10, we present 2D scatter plots of the maximum a posteriori (MAP) estimates<sup>16</sup> of the reconstructed Ly $\alpha$  emission-line parameters compared to the originally obtained values from the full MCMC fit to the QSO (without masking out the Ly $\alpha$  line). For each of the six Ly $\alpha$  emission-line parameters, we highlight the 68 and 95 percentiles of the joint marginalized likelihoods for the distributions by the green solid and dashed contours, respectively. Additionally, the red dashed curve demarcates the one-to-one line, along which all QSOs would sit if the reconstruction profile worked idealistically.

Across the six Ly $\alpha$  panels, we find strong agreement ( $\rho > 0.7$ ) amongst half of our Ly $\alpha$  line parameters, those being the peak amplitudes of both the Ly $\alpha$  broad and narrow components and the velocity offset for the Ly $\alpha$  narrow-line component. For the remainder of the parameters, we find moderate to weaker recovery of the original line parameters. However, note that in order to keep this figure as clear as possible, we are only providing the MAP estimates. Within Figs 8 and 9, we found that the relative scatter on the reconstructed Ly $\alpha$  line profile parameters was notable and therefore the majority of the reconstructed parameters are within the 68 per cent marginalized errors.

The reconstructed Ly $\alpha$  profile parameters highlighted here reflect the correlations recovered from the covariance matrix in Fig. 2. We found strong correlations in the peak amplitudes of the Ly $\alpha$  profiles and the narrow component velocity offset. The lack of a strong correlation for the width of the Ly $\alpha$  line in our covariance matrix translates to weaker recovery of these parameters. In principle, these weaker correlations could be further strengthened by adding an appropriate prior on the linewidths motivated by the statistical distributions recovered from the full sample or other line properties such as correlations between the equivalent widths.

<sup>16</sup> Note that throughout this work, the recovered MAP estimates from the full posterior distribution do not differ significantly from the peak of the associated marginalized PDFs.

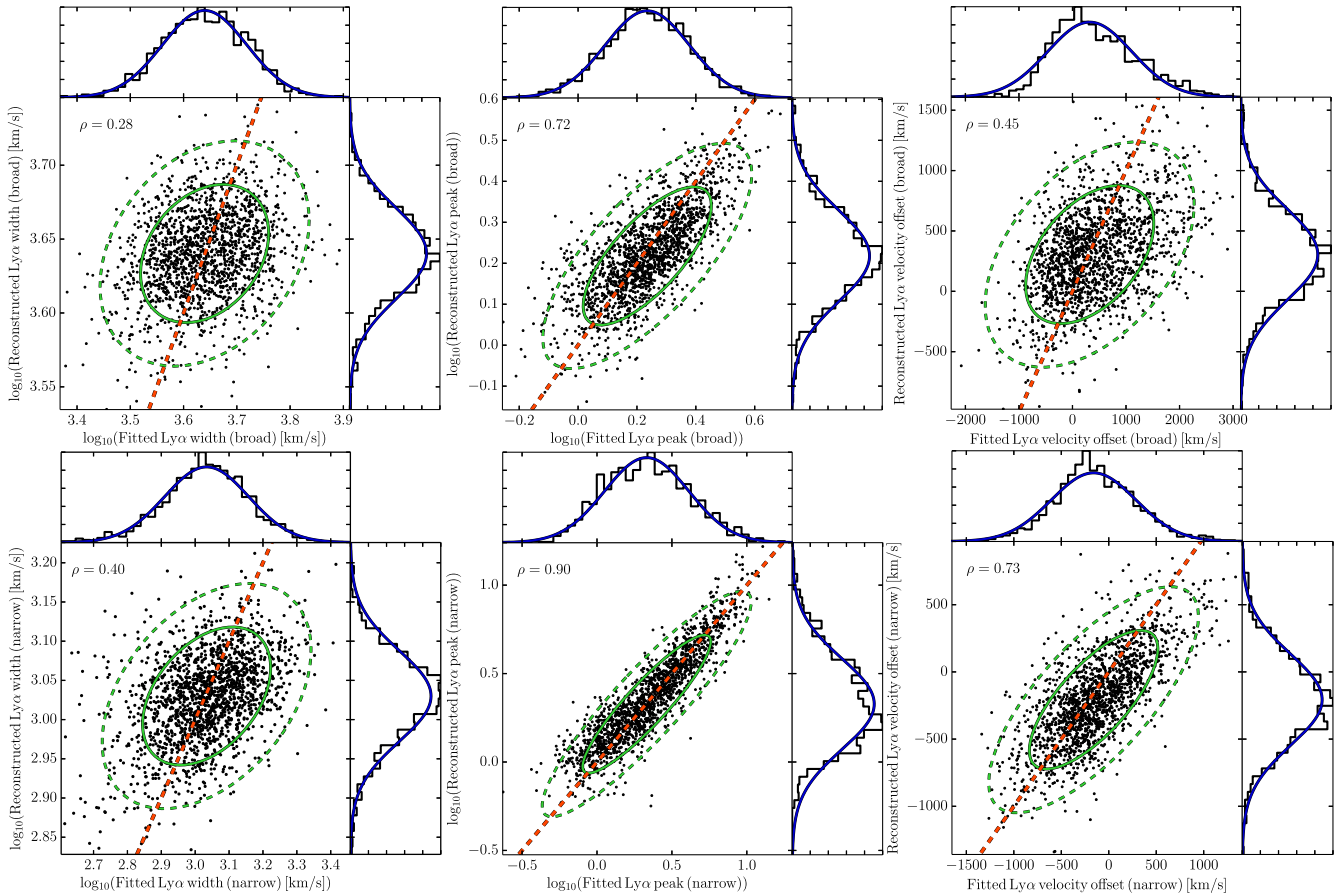


**Figure 10.** A visual characterization of the performance of the Ly $\alpha$  emission-line reconstruction pipeline at recovering each of the six Ly $\alpha$  line parameters. We provide the 2D scatter between the full MCMC fits to the QSOs, compared to the reconstructed values from a fit to the same QSO masking the Ly $\alpha$  region (flux masked at  $\lambda < 1275 \text{ \AA}$ ) and applying our additional prior on the QSO flux near  $\lambda = 1230 \text{ \AA}$ . Green solid and dashed contours enclose the 68 and 95 per cent scatter of the reconstructed Ly $\alpha$  parameters relative to their expected (true) value, while the red dashed curves correspond to the one-to-one line on which all points would lie if the reconstruction procedure worked perfectly. Histograms (black curves) correspond to the one-dimensional PDFs of the Ly $\alpha$  parameters from the full MCMC fitting (top) and the recovered estimate from the reconstruction pipeline fit to the Ly $\alpha$  masked QSO (right). Blue curves represent the associated Gaussian distribution with equivalent scatter. Note that the peak amplitude is normalized by  $f_{1450}$  and is therefore dimensionless.

In Fig. 10, there is also slight evidence for a bias in the reconstructed parameters, as highlighted by the orientation of the green contours (68 and 95 percentiles of the reconstructed parameter distributions) relative to the reference one-to-one line. However, this could artificially arise as the increase/decrease in any one of these Ly $\alpha$  line parameters could be compensated for by respective changes in others (i.e. model degeneracies), whereas the full six-dimensional Ly $\alpha$  likelihood function takes these model degeneracies into account when estimating the full reconstructed Ly $\alpha$  profile.

In order to better illustrate the full reconstruction of the joint Ly $\alpha$  parameter likelihoods, in Fig. 11, we show the information from the six individual Ly $\alpha$  line parameters as a single, total measured Ly $\alpha$  line flux at two arbitrarily defined locations blue (1205  $\text{\AA}$ ) and redward (1220  $\text{\AA}$ ) of the Ly $\alpha$  line centre. We compare the total reconstructed Ly $\alpha$  line flux against the measured Ly $\alpha$  line flux from our full fit to the same QSO, providing the reference one-to-one relation as the red dashed curve and the grey shaded region encompasses the region in which the reconstructed Ly $\alpha$  line flux is within 15 per cent of the measured flux. Immediately obvious from this figure is that there are no apparent biases in the reconstruction process, i.e. we neither systematically over nor underestimate the

reconstructed Ly $\alpha$  line profile. This figure highlights the strength of the Ly $\alpha$  reconstruction process. Redward of Ly $\alpha$  (at 1220  $\text{\AA}$ ), closer to our flux prior at 1230  $\text{\AA}$ , we find that  $\sim 90$  per cent of all reconstructed Ly $\alpha$  line profiles have a recovered flux within 15 per cent. As one would expect, the scatter increases blueward of Ly $\alpha$  (at 1205  $\text{\AA}$ ); however, we still find the reconstructed Ly $\alpha$  line flux to be within 15 per cent for  $\sim 85$  per cent of our sampled QSOs. This highlights statistically that the reconstruction process performs an excellent job of recovering the full Ly $\alpha$  line profile.

## 6 POTENTIAL APPLICATIONS

In this work, we have developed an MCMC fitting algorithm for the sole purpose of characterizing the QSO continuum and the emission-line profiles within the range  $1180 \text{ \AA} < \lambda < 2300 \text{ \AA}$ . Our goal was the construction of a covariance matrix to reconstruct the Ly $\alpha$  line profile. However, due to the flexibility of the MCMC approach, many other applications could benefit from such a pipeline.

First, we were only interested in correlations amongst the strongest, high-ionization emission-line parameters for our covariance matrix. However, various properties of QSOs can be extracted from accurate recovery of the linewidths and ratios. For

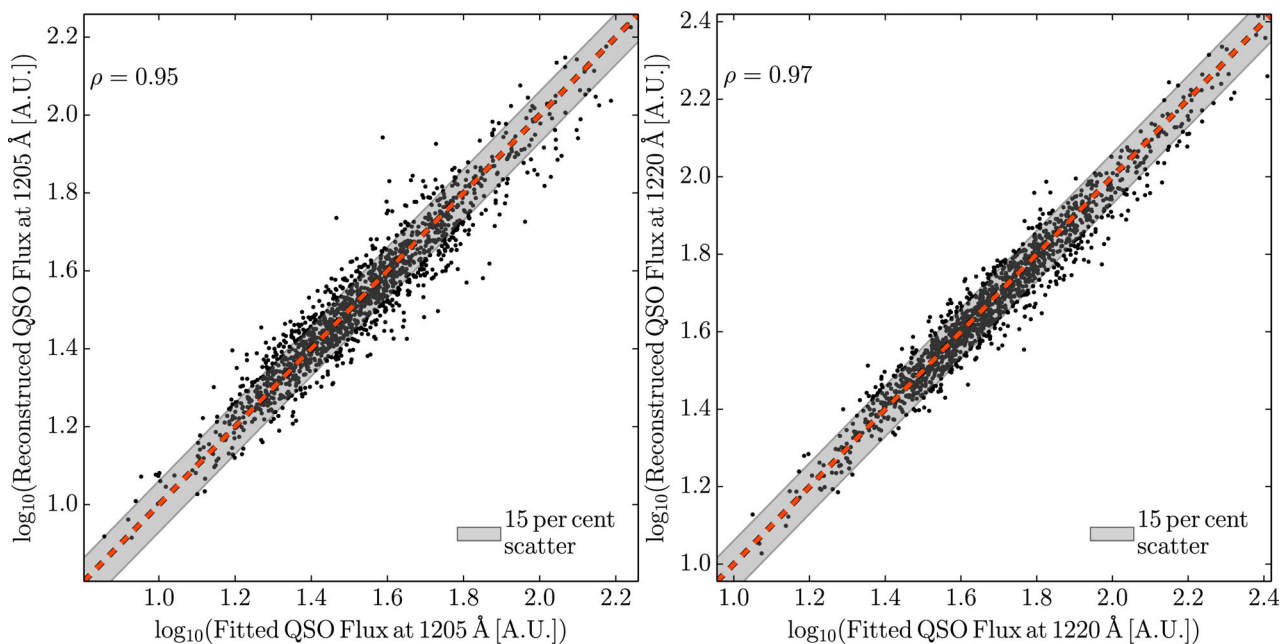


**Figure 11.** A comparison of the maximum likelihood reconstructed Ly $\alpha$  line flux (including the flux prior; Section 5.3) to the actual Ly $\alpha$  line flux obtained from the full fit at a specific wavelength for each QSO within our ‘good’ sample (1673 QSOs; we define  $1 \text{ au} = 10^{-17} \text{ erg cm}^{-2} \text{ s}^{-1} \text{ \AA}^{-1}$ ). Left-hand panel: blueward of Ly $\alpha$  ( $\lambda = 1205 \text{ \AA}$ ). Right-hand panel: redward ( $\lambda = 1220 \text{ \AA}$ ). The red dashed curve corresponds to the one-to-one relation and the grey shaded region encompasses 15 per cent scatter in the reconstructed Ly $\alpha$  flux relative to the actual measured Ly $\alpha$  line flux. At  $\lambda = 1220 \text{ \AA}$ , we find the reconstructed Ly $\alpha$  line flux to be within 15 per cent of the actual Ly $\alpha$  line flux in  $\sim 90$  per cent of all QSOs, decreasing to  $\sim 85$  per cent at  $\lambda = 1205 \text{ \AA}$ .

example, the QSO metallicity has been estimated from measuring the N v/C iv, N v/He ii and the Si iv + O iv/C iv line ratios in samples of QSOs from Nagao, Marconi & Maiolino (2006a) ( $2 < z < 4.5$ ) and Juarez et al. (2009) ( $4 < z < 6.4$ ). Using the same line ratios, we could recover estimates for the metallicities for all QSOs within our measured sample.

Several other emission-line ratios (e.g. the R23 parameter, [O iii]/[O ii], C iv/He ii, N-based ratios) can additionally be used as proxies for QSO metallicity (e.g. Nagao, Maiolino & Marconi 2006b; Matsuoka et al. 2009; Batra & Baldwin 2014). By extending our QSO MCMC framework, many other emission lines can be obtained and characterized to improve the QSO metallicity estimates. Crucially, this MCMC approach would enable a large data set of QSOs to be rapidly explored. The extension to measuring the metallicities of the QSOs would enable quantities such as the SMBH mass to be recovered through existing correlations between the emission-line FWHMs.

In Section 3.3, we have outlined our method to identify and fit absorption features (see e.g. Zhu & Ménard 2013 for a more robust approach). While, in this work, these have been considered contaminants, the prevalence and measurement of these lines could be used to infer properties of the metallicities within intervening absorbers (e.g. Ryan-Weber, Pettini & Madau 2006; Becker, Rauch & Sargent 2009; D’Odorico et al. 2013) and to reveal the presence of massive outflows of ionized gas from their nuclei (e.g. Crenshaw, Kraemer & George 2003, and reference therein). For example, we have thrown out any QSOs with strong intervening absorption from systems such as DLAs; however, analysing these sources with our MCMC fitting algorithm could yield measurements on the internal properties of these absorption systems.

Assuming the input quasars to our MCMC are representative of the quasar population as a whole and further that the UV spectral properties of quasars do not evolve with redshift, our model can be

used to predict the intrinsic distribution of quasar spectra at redshifts beyond those from which the model was calibrated ( $z \sim 2.5$ ). A similar procedure has been often employed to characterize the colour selection efficiency of quasar surveys (e.g. Fan 1999), although the correlations obtained through our MCMC approach provide more detailed reconstruction of quasar emission features and hence more reliable colour models. Particularly, since the Ly $\alpha$  line plays such a key role in the selection of high- $z$  quasars, our model could be used to identify quasars missing from current surveys due to selection effects and provide more robust statistics for high- $z$  quasar luminosity functions.

In addition, by recovering an estimate for the intrinsic Ly $\alpha$  emission-line profile, one can investigate the QSO proximity effect. This approach requires an estimate of the intrinsic QSO luminosity, coupled with the modelling of the Ly $\alpha$  forest. Within the sphere of influence of the QSO, the photoionization background is higher than the mean background permeating the IGM. Modelling the transition between the mean IGM background and the drop-off in QSO luminosity has been used by several authors to recover estimates of the photoionization background in the IGM (e.g. Bolton et al. 2005; Bolton & Haehnelt 2007b; Calverley et al. 2011). At the redshifts where these studies have been performed (e.g.  $2 < z < 6$ ), the Ly $\alpha$  line profile is not obscured or attenuated by a neutral IGM. Therefore, one could, in principle, push the flux prior we used in this work much closer to the Ly $\alpha$  line centre, to substantially reduce the errors on the intrinsic Ly $\alpha$  emission-line profile blueward of Ly $\alpha$ .

At  $z > 6$ , for an increasingly neutral IGM, the intrinsic Ly $\alpha$  emission line can become increasingly attenuated by the Gunn–Peterson IGM damping wing. While existing methods have been developed to access information on the red side of Ly $\alpha$  (e.g. Kramer & Haiman 2009), for the  $z = 7.1$  QSO ULASJ1120+0641 (Mortlock et al. 2011), evidence suggests that the IGM damping wing imprint extends further redward (e.g. Bolton et al. 2011; Mortlock

et al. 2011), limiting the effectiveness of these approaches. The approach developed in this work should be unaffected by this as here we do not fit the Ly $\alpha$  line, our reconstruction method therefore is perfectly suited for exploring the potential imprint of the IGM damping wing on the  $z = 7.1$  QSO (e.g. Greig et al. 2016), along with other future  $z > 6$  QSOs.

## 7 CONCLUSION

Characterizing the continuum and emission-line properties of QSOs provides a wealth of information on the internal properties of the AGN, such as the mass of the SMBH, the QSO metallicity, star formation rates of the host galaxy, nuclear outflows and winds, etc. Furthermore, the intrinsic Ly $\alpha$  line shape can be used to probe properties of the IGM, such as the mean photoionization background and the abundance of neutral hydrogen in the IGM at  $z > 6$ .

Motivated by correlations amongst QSO emission lines (e.g. Boroson & Green 1992; Sulentic, Marziani & Dultzin-Hacyan 2000; Shen et al. 2011), in this work, we developed a new reconstruction method to recover the intrinsic Ly $\alpha$  profile. This method is based on the construction of a covariance matrix built from a large sample of moderate- $z$  ( $2.0 < z < 2.5$ ), high S/N ( $S/N > 15$ ) QSOs from the BOSS observational programme. We use this moderate- $z$  sample to characterize the intrinsic Ly $\alpha$  line profile, where it should be relatively unaffected by intervening neutral hydrogen in the IGM. In order to characterize each QSO within our sample, we developed an MCMC fitting algorithm to jointly fit the QSO continuum, the emission lines and any absorption features that could contaminate or bias the fitting of the QSO. We modelled the QSO continuum as a single two parameter power law ( $\propto \lambda^{\alpha_2}$ ) and each emission line is modelled as a Gaussian defined by three parameters, its width, peak amplitude and velocity offset from systemic.

We constructed our covariance matrix from a refined sample of 1673 QSOs, using the high-ionization emission lines Ly $\alpha$ , Si IV + O IV], C IV and C III]. Owing to the flexibility of the MCMC framework, we explored various combinations of single and double component Gaussians to characterize these lines. For Ly $\alpha$  and C IV, we settled on a double component Gaussian, to model the presence of a broad and narrow component. For the remaining two lines, we considered a single component. This resulted in an  $18 \times 18$  covariance matrix, which we used to investigate new and existing correlations amongst the line profiles. We identified several strong trends from our covariance matrix, most notably the strong positive correlation between the peak amplitudes of the Ly $\alpha$  and C IV narrow components ( $\rho = 0.8$ ) and the strong anticorrelation between the Ly $\alpha$  narrow component peak amplitude and the width of the C III] line ( $\rho = -0.74$ ). These two were the strongest examples of a consistent trend of a positive correlation in the peak amplitudes across all the emission-line species and the anticorrelation between the peak amplitudes and linewidths.

Using this covariance matrix, we constructed an  $N$ -dimensional Gaussian likelihood function from which we are able to recover our reconstructed Ly $\alpha$  line profile. The reconstruction method works as follows.

(i) Fit a QSO with our MCMC pipeline within the range  $1275 \text{ \AA} < \lambda < 2300 \text{ \AA}$ , recovering the parameters defining the QSO continuum and the Si IV + O IV], C IV and C III] lines.

(ii) Obtain a six-dimensional estimate of the reconstructed Ly $\alpha$  line profile (modelled as a two component Gaussian) that provides the best-fitting profile and correlated uncertainties, by evaluating the  $N$ -dimensional likelihood function describing our full covariance

matrix including a prior on the reconstructed Ly $\alpha$  line using the observed QSO flux within the range  $1230 < \lambda < 1275 \text{ \AA}$ .

To visually demonstrate the performance of this reconstruction method, we applied it to a randomly selected QSO from our full data set. Finally, we quantitatively assessed its performance by applying it to the full QSO sample and compared the reconstructed Ly $\alpha$  profile parameters to those recovered from the original full MCMC fit of the same QSO. We found that estimates for both the Ly $\alpha$  peak amplitudes are recovered strongly, as is the velocity offset of the narrow-line component. For both of the linewidths and the broad component velocity offset, we find moderate agreement. We additionally explored the total reconstructed Ly $\alpha$  flux (rather than individual parameters) relative to the original full MCMC fit at two distinct wavelengths blueward ( $1205 \text{ \AA}$ ) and redward ( $1220 \text{ \AA}$ ) of Ly $\alpha$ . Our reconstruction method recovered the Ly $\alpha$  line flux to within 15 per cent of the measured flux at  $1205 \text{ \AA}$  ( $1220 \text{ \AA}$ )  $\sim 85$  ( $\sim 90$ ) per cent of the time.

There are several potential applications for both the MCMC fitting method and the Ly $\alpha$  reconstruction pipeline. The MCMC fitting could be easily modified to measure any emission or absorption feature within a QSO spectrum. With this, many properties of the source QSO could be extracted, for example, QSO metallicities. The ability to reconstruct the intrinsic Ly $\alpha$  line profile could have important cosmological consequences, such as improving estimates of the IGM photoionization background or recovering estimates of the IGM neutral fraction.

## ACKNOWLEDGEMENTS

We thank the anonymous referee for their helpful suggestions. AM and BG acknowledge funding support from the European Research Council (ERC) under the European Union's Horizon 2020 research and innovation programme (grant agreement No 638809 – AIDA – PI: AM). ZH is supported by NASA grant NNX15AB19G.

Funding for SDSS-III has been provided by the Alfred P. Sloan Foundation, the Participating Institutions, the National Science Foundation and the US Department of Energy Office of Science. The SDSS-III web site is <http://www.sdss3.org/>.

SDSS-III is managed by the Astrophysical Research Consortium for the Participating Institutions of the SDSS-III Collaboration including the University of Arizona, the Brazilian Participation Group, Brookhaven National Laboratory, Carnegie Mellon University, University of Florida, the French Participation Group, the German Participation Group, Harvard University, the Instituto de Astrofísica de Canarias, the Michigan State/Notre Dame/JINA Participation Group, Johns Hopkins University, Lawrence Berkeley National Laboratory, Max Planck Institute for Astrophysics, Max Planck Institute for Extraterrestrial Physics, New Mexico State University, New York University, Ohio State University, Pennsylvania State University, University of Portsmouth, Princeton University, the Spanish Participation Group, University of Tokyo, University of Utah, Vanderbilt University, University of Virginia, University of Washington and Yale University.

## REFERENCES

- Akeret J., Seehars S., Amara A., Refregier A., Csillaghy A., 2013, *Astron. Comput.*, 2, 27
- Alam S. et al., 2015, *ApJS*, 219, 12
- Baldwin J. A., 1977, *ApJ*, 214, 679
- Baldwin J., Ferland G., Korista K., Verner D., 1995, *ApJ*, 455, L119
- Baldwin J. A. et al., 1996, *ApJ*, 461, 664

- Barkana R., 2002, *New Astron.*, 7, 85
- Batra N. D., Baldwin J. A., 2014, *MNRAS*, 439, 771
- Becker G. D., Rauch M., Sargent W. L. W., 2009, *ApJ*, 698, 1010
- Becker G. D., Hewett P. C., Worseck G., Prochaska J. X., 2013, *MNRAS*, 430, 2067
- Blandford R. D., McKee D. F., 1982, *ApJ*, 255, 419
- Bolton J. S., Haehnelt M. G., 2007a, *MNRAS*, 374, 493
- Bolton J. S., Haehnelt M. G., 2007b, *MNRAS*, 382, 325
- Bolton J. S., Haehnelt M. G., Viel M., Springel V., 2005, *MNRAS*, 357, 1178
- Bolton J. S., Haehnelt M. G., Warren S. J., Hewett P. C., Mortlock D. J., Venemans B. P., McMahon R. G., Simpson C., 2011, *MNRAS*, 416, L70
- Bolton A. S. et al., 2012, *AJ*, 144, 144
- Boroson T. A., Green R. F., 1992, *ApJS*, 80, 109
- Bosman S. E. I., Becker G. D., 2015, *MNRAS*, 452, 1105
- Bovy J. et al., 2011, *ApJ*, 729, 141
- Brotherton M. S., Tran H. D., Becker R. H., Gregg M. D., Laurent-Muehleisen S. A., White R. L., 2001, *ApJ*, 546, 775
- Calverley A. P., Becker G. D., Haehnelt M. G., Bolton J. S., 2011, *MNRAS*, 412, 2543
- Carilli C. L. et al., 2010, *ApJ*, 714, 834
- Corbin M. R., Boroson T. A., 1996, *ApJS*, 107, 69
- Crenshaw D. M., Kraemer S. B., George I. M., 2003, *ARA&A*, 41, 117
- D’Odorico V. et al., 2013, *MNRAS*, 435, 1198
- Dawson K. S. et al., 2013, *AJ*, 145, 10
- Dietrich M., Hamann F., Shields J. C., Constantin A., Vestergaard M., Chaffee F., Foltz C. B., Junkkarinen V. T., 2002, *ApJ*, 581, 912
- Dijkstra M., 2014, *Publ. Astron. Soc. Astron.*, 31, e040
- Dodelson S., Schneider M. D., 2013, *Phys. Rev. D*, 88, 063537
- Eisenstein D. J. et al., 2011, *AJ*, 142, 72
- Fan X., 1999, *AJ*, 117, 2528
- Fan X. et al., 2006, *AJ*, 132, 117
- Fitzpatrick E. L., 1999, *PASP*, 111, 63
- Font-Ribera A. et al., 2013, *J. Cosmol. Astropart. Phys.*, 05, 018
- Foreman-Mackey D., Hogg D. W., Lang D., Goodman J., 2013, *PASP*, 125, 306
- Francis P. J., Hewett P. C., Foltz C. B., Chaffee F. H., Weymann R. J., Morris S. L., 1991, *ApJ*, 373, 465
- Francis P. J., Hewett P. C., Foltz C. B., Chaffee F. H., 1992, *ApJ*, 398, 476
- Gallerani S., Ferrara A., Fan X., Choudhury R. T., 2008, *MNRAS*, 386, 359
- Goodman J., Weare J., 2010, *Commun. Appl. Math. Comput. Sci.*, 5, 1
- Greig B., Mesinger A., Haiman Z., Simcoe R. A., 2016, *MNRAS*, preprint ([arXiv:1606.00441](https://arxiv.org/abs/1606.00441))
- Gunn J. E. et al., 2006, *AJ*, 131, 2332
- Harris D. W. et al., 2016, *ApJ*, 151, 155
- Hewett P. C., Wild V., 2010, *MNRAS*, 405, 2302
- Hopkins P. F. et al., 2004, *AJ*, 128, 1112
- Juarez Y., Maiolino R., Mujica R., Pedani M., Marinoni S., Nagao T., Marconi A., Oliva E., 2009, *A&A*, 494, L25
- Kaspi S., Smith P. S., Netzer H., Maoz D., Jannuzi B. T., Giveon U., 2000, *ApJ*, 533, 631
- Kirkpatrick J. A., Schlegel D. J., Ross N. P., Myers A. D., Hennawi J. F., Sheldon E. S., Schneider D. P., Weaver B. A., 2011, *ApJ*, 743, 125
- Kramer R. H., Haiman Z., 2009, *MNRAS*, 400, 1493
- Lee K.-G., Spergel D. N., 2011, *ApJ*, 734, 21
- Liddle A. R., 2004, *MNRAS*, 351, L49
- McDonald P., Eisenstein D. J., 2007, *Phys. Rev. D*, 76, 63009
- McGreer I. D., Mesinger A., D’Odorico V., 2015, *MNRAS*, 447, 499
- McLean I. S. et al., 2010, in McLean I. S., Ramsay S. K., Takami H., eds, *Proc. SPIE Conf. Ser. Vol. 7735, Ground-based and Airborne Instrumentation for Astronomy III*. SPIE, Bellingham, p. 77351E
- McLean I. S. et al., 2012, in McLean I. S., Ramsay S. K., Takami H., eds, *Proc. SPIE Conf. Ser. Vol. 8446, Ground-based and Airborne Instrumentation for Astronomy IV*. SPIE, Bellingham, p. 84460J
- Margala D., Kirkby D., Dawson K., Bailey S., Blanton M., Schneider D. P., 2015, *ApJ*, 831, 157
- Matsuoka K., Nagao T., Maiolino R., Marconi A., Taniguchi Y., 2009, *A&A*, 503, 721
- Mesinger A., 2010, *MNRAS*, 407, 1328
- Mesinger A., Haiman Z., 2004, *ApJ*, 611, L69
- Mesinger A., Haiman Z., 2007, *ApJ*, 660, 923
- Miralda-Escudé J., 1998, *ApJ*, 501, 15
- Mortlock D. J. et al., 2011, *Nature*, 474, 616
- Nagao T., Marconi A., Maiolino R., 2006a, *A&A*, 447, 157
- Nagao T., Maiolino R., Marconi A., 2006b, *A&A*, 459, 85
- Pâris I. et al., 2011, *A&A*, 530, A50
- Pâris I. et al., 2016, *A&A*, 530, A50
- Peebles P. J. E., 1993, *Principles of Physical Cosmology*. Princeton Univ. Press, Princeton, NJ
- Peterson B. M., 1993, *PASP*, 105, 1084
- Peterson B. M. et al., 2004, *ApJ*, 613, 682
- Petri A., May M., Haiman Z., 2016, *Phys. Rev. D*, 94, 063534
- Planck Collaboration XIII, 2015, *A&A*, 594, A13
- Planck Collaboration XLVI, 2016, *A&A*, 596, A107
- Planck Collaboration XLVII, 2016, *A&A*, 596, A108
- Rauch M., 1998, *ARA&A*, 36, 267
- Richards G. T. et al., 2003, *AJ*, 126, 1131
- Richards G. T. et al., 2011, *AJ*, 141, 167
- Ross N. P. et al., 2012, *ApJS*, 199, 3
- Ryan-Weber E. V., Pettini M., Madau P., 2006, *MNRAS*, 371, L78
- Schroeder J., Mesinger A., Haiman Z., 2013, *MNRAS*, 428, 3058
- Schwarz G., 1978, *Ann. Stat.*, 461, 6
- Scott J. E., Kriss G. A., Brotherton M., Green R. F., Hutchings J., Shull J. M., Zheng W., 2004, *ApJ*, 615, 135
- Shang Z., Wills B. J., Wills D., Brotherton M. S., 2007, *AJ*, 134, 294
- Shen Y., Ménard B., 2012, *ApJ*, 748, 131
- Shen Y., Greene J. E., Strauss M. A., Richards G. T., Schneider D. P., 2008, *ApJ*, 680, 169
- Shen Y. et al., 2011, *ApJS*, 194, 45
- Shull J. M., Stevans M., Danforth C. W., 2012, *ApJ*, 752, 162
- Smee S. A. et al., 2013, *AJ*, 146, 32
- Stevans M., Shull J. M., Danforth C. W., Tilton E. M., 2014, *ApJ*, 794, 75
- Sulentic J. W., Marziani P., Dultzin-Hacyan D., 2000, *ARA&A*, 38, 521
- Suzuki N., 2006, *ApJS*, 163, 110
- Suzuki N., Tytler D., Kirkman D., O’Meara J. M., Lubin D., 2005, *ApJ*, 618, 592
- Taylor A., Joachimi B., 2014, *MNRAS*, 442, 2728
- Telfer R. C., Zheng W., Kriss G. A., Davidsen A. F., 2002, *ApJ*, 565, 773
- Vanden Berk D. E. et al., 2001, *AJ*, 122, 549
- Vernet J. et al., 2011, *A&A*, 536, 105
- Vestergaard M., Peterson B. M., 2006, *ApJ*, 641, 689
- Vestergaard M., Wilkes B. J., 2001, *ApJS*, 134, 1
- White M., 2003, *The Davis Meeting On Cosmic Inflation*. p. 18, preprint ([arXiv:astro-ph/0305474](https://arxiv.org/abs/astro-ph/0305474))
- Wills B. J., Brotherton M. S., Fang D., Steidel C. C., Sargent W. L. W., 1993, *ApJ*, 415, 563
- Wyithe J. S. B., Bolton J. S., 2011, *MNRAS*, 412, 1926
- Wyithe J. S. B., Loeb A., 2004, *ApJ*, 612, 597
- Zhu G., Ménard B., 2013, *ApJ*, 770, 130

## APPENDIX A: SELECTING THE SYSTEMIC REDSHIFT FOR OUR BOSS SAMPLE

The reconstruction method discussed within this work is strongly dependent on having an accurate systemic redshift for the QSO sample. In the absence of knowing the true source redshift, systematic errors in its estimation will filter into the recovered line profile parameters, most notably the velocity offset of the line centre. As a result, this will affect any reported line profile correlations that are necessary for the Ly $\alpha$  line profile reconstruction. Within this appendix, we discuss our attempts to determine the most robust and accurate redshift to be adopted within this work.

The BOSS DR12Q data base (Pâris et al. 2016) provides six available redshift estimates; a visually inspected redshift,  $z_{VI}$ , the

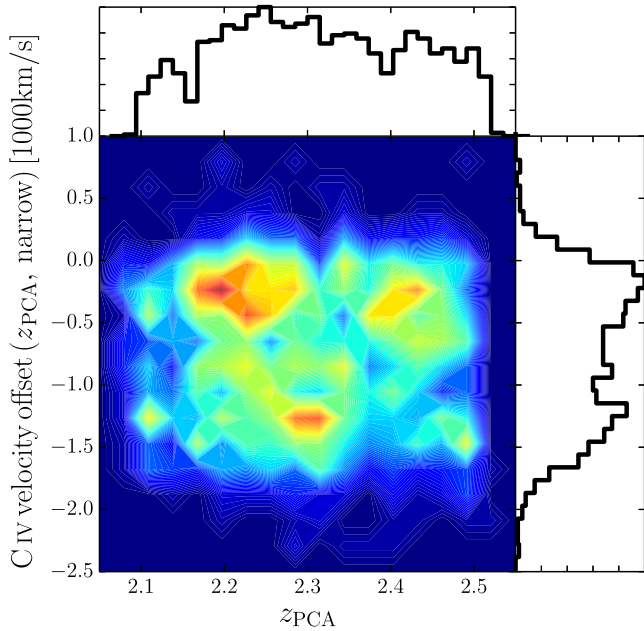


**Figure A1.** Distribution of the velocity offset from the C IV narrow component against the estimated PCA redshift,  $z_{\text{PCA}}$ , for our ‘good’ sample of 1673 QSOs. In the central panel is a two-dimensional histogram normalized to unity, with red denoting the highest density of QSOs. In the top (right) panels are the one-dimensional histograms for the distribution of  $z_{\text{PCA}}$  (C IV narrow-line component velocity offset).

BOSS pipeline redshift based on a decomposed eigenvalue training set,  $z_{\text{pipeline}}$  (see e.g. Bolton et al. 2012), an automated PCA based approach,  $z_{\text{PCA}}$ , and three other estimates determined from the location of the peak emission for the individual line profiles,  $z_{\text{CIV}}$ ,  $z_{\text{CIII}}$  and  $z_{\text{MgII}}$ . Using the earlier DR9Q data base, Font-Ribera et al. (2013) performed a detailed analysis on each of these redshift estimates. These authors found  $z_{\text{PCA}}$  to be the optimal redshift estimator, returning both the smallest dispersion and bias amongst these six available measurements.

However, in adopting  $z_{\text{PCA}}$  as the optimal redshift estimator, we find a bias within our selected sample of QSOs. In Fig. A1, we show the velocity offset of the narrow component of the C IV line (measured with  $z_{\text{PCA}}$ ) as a function of the estimated redshift from the PCA approach using our ‘good’ sample of 1673 QSOs. In the rightmost panel, we show the one-dimensional histogram for the narrow component of C IV. Immediately obvious from this figure is the non-Gaussian (bi-modal) nature of the distribution. Contrast this with the equivalent figure of the narrow component of C IV for the  $z_{\text{pipeline}}$  redshift estimator shown in Fig. A2, which shows no obvious departure from Gaussianity. We have additionally tested this for the other redshift estimators (e.g.  $z_{\text{VI}}$  and  $z_{\text{MgII}}$ ) and found no evidence for the same bi-modal distribution as shown by  $z_{\text{PCA}}$ .

In the central panel of Fig. A1, we show the two-dimensional histogram, with red signifying the highest density of QSOs. Presenting the data in this manner immediately highlights the source of error. The two peaks in the C IV velocity offset distribution are driven by two separate, discrete regions within the C IV– $z_{\text{PCA}}$  parameter space: the primary peak in the C IV velocity offset at  $\sim -250 \text{ km s}^{-1}$  (for all redshifts except the ‘hole’ at  $z \sim 2.3$ ) and the secondary peak at  $\sim -1250 \text{ km s}^{-1}$  (at  $z \sim 2.3$ ). This discrete ‘overdensity’ of QSOs at  $z \sim 2.3$  is most likely an unphysical artefact. The likely cause of this discrete transition near  $z \sim 2.3$  is the redshifting of the Mg II line between strong OH sky line features. Typically, the

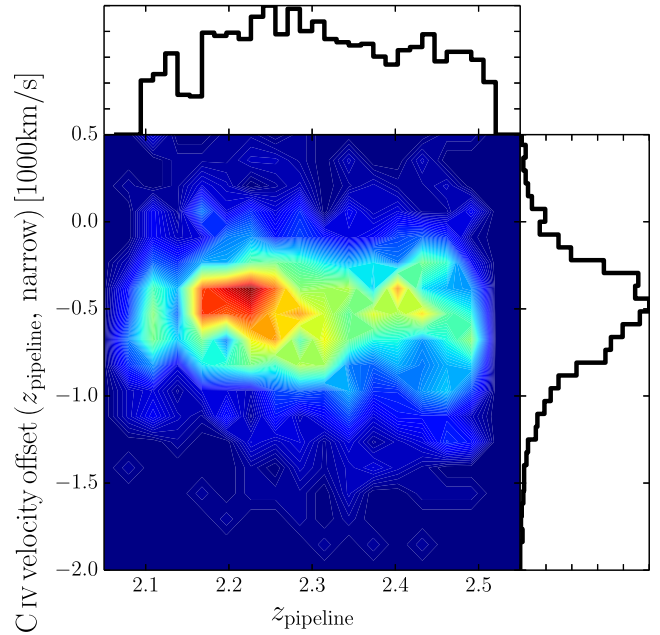


**Figure A2.** Same as Fig. A1, except showing the C IV narrow component measured from the  $z_{\text{pipeline}}$  redshift estimator.

Mg II emission line is one of the strongest anchors in which the source redshift can be determined. At  $2.25 \lesssim z \lesssim 2.33$ , Mg II is observed within a region that has a relatively low sky background with few sky lines, resulting in a higher Mg II S/N. However, at  $z \lesssim 2.25$  and  $z \gtrsim 2.33$ , the Mg II feature appears amongst OH forest regions with very strong sky lines, resulting both in a noisier signal and it being strongly affected by systematics owing to the sky line residuals. Therefore, the weakening of the Mg II information in determining the QSO redshift within the PCA approach at  $z \gtrsim 2.33$  is the likely cause of this transition. Due to this bi-modal nature, which appears to be intrinsic only to the  $z_{\text{PCA}}$  redshift estimator, and since throughout this work we have assumed the distributions of line profiles can all be represented by a Gaussian distribution, we refrain from adopting the PCA redshift within this analysis.

The next three best candidates after  $z_{\text{PCA}}$  from the Font-Ribera et al. (2013) analysis are  $z_{\text{VI}}$ ,  $z_{\text{pipeline}}$  and  $z_{\text{MgII}}$ .<sup>17</sup> Of these three,  $z_{\text{MgII}}$  has the smallest bias, followed by  $z_{\text{pipeline}}$  and  $z_{\text{VI}}$ . In contrast,  $z_{\text{VI}}$  has the smallest dispersion, followed by  $z_{\text{pipeline}}$  and  $z_{\text{MgII}}$ . In this work, we do not consider using the visually inspected redshift as: (i) it has the strongest systematic bias of these choices and (ii) it is the least objective measure (not entirely automated), requiring intervention to improve the redshift.

The QSOs within our ‘good’ sample are selected within  $2.08 \leq z \leq 2.5$ . By adopting,  $z_{\text{MgII}}$  instead of  $z_{\text{pipeline}}$ , we lose all QSOs above  $z > 2.4$ , where no  $z_{\text{MgII}}$  redshift is reported for any of the sources in DR12Q. Ultimately, the loss of sources reduces the total number of QSOs within our sample by  $\sim 25$  per cent. Despite the reduction in sample size, the  $z_{\text{MgII}}$  and  $z_{\text{pipeline}}$  samples return almost identical covariance matrices, signifying consistency in both redshift estimates. The major difference between the two samples is the notably stronger correlation in the velocity offsets for the emission-line

<sup>17</sup> We do not consider either of  $z_{\text{CIV}}$  or  $z_{\text{CIII}}$  as these have the largest dispersion and bias.

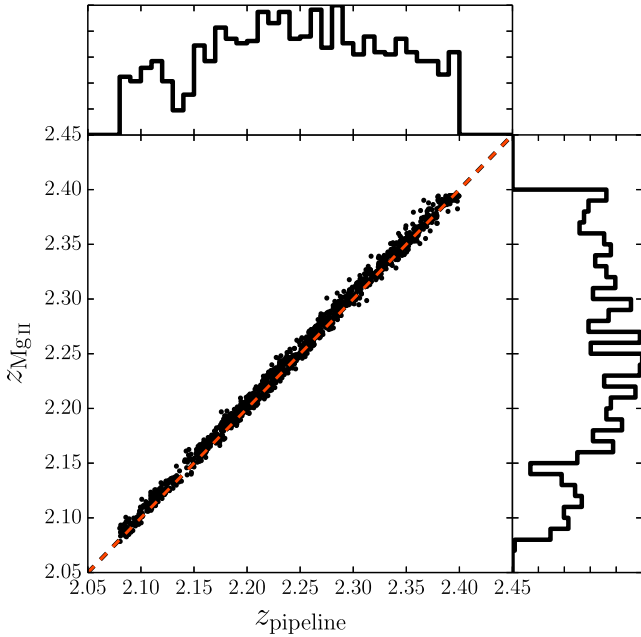


**Figure A3.** The distribution of 1274 QSOs drawn from our ‘good’ sample which contain both a Mg II and BOSS pipeline redshift. Top and left-hand panels are histograms of the BOSS pipeline redshift,  $z_{\text{pipeline}}$  and Mg II derived redshift,  $z_{\text{Mg II}}$ . The red dashed curve denotes the one-to-one relation, highlighting a slight offset between the two redshift estimates.

parameters within the  $z_{\text{Mg II}}$ . However, this is to be expected owing to the differences in how the redshifts are estimated. For  $z_{\text{Mg II}}$ , a single line profile is used to estimate the redshift, whereas in  $z_{\text{pipeline}}$ , several line profiles are compared to a training set to estimate the best candidate redshift. By using several line profiles to determine the source redshift, intrinsic scatter within the source spectrum can cause the redshift estimates to deviate compared to those from a single line measurement such as  $z_{\text{Mg II}}$ . Despite  $z_{\text{Mg II}}$  providing the stronger line profile components for the velocity offsets than the  $z_{\text{pipeline}}$ , we refrain from using the Mg II redshifts as these correlations may be artificially high owing to their estimation from only a single line profile. We deem the correlations from  $z_{\text{pipeline}}$  sample to be more conservative, while also benefitting from the addition of maintaining a larger statistical sample.

Finally,  $z_{\text{Mg II}}$  and  $z_{\text{pipeline}}$  return relatively similar dispersions, with  $z_{\text{Mg II}}$  being less biased. With the vast majority of the QSOs in our sample having both redshifts, in principle, we can attempt to calibrate our  $z_{\text{pipeline}}$  sample by the  $z_{\text{Mg II}}$  sample. In Fig. A3, we provide the  $z_{\text{Mg II}}-z_{\text{pipeline}}$  parameter space, with the red dashed curve denoting the one-to-one relation, from which one can see a small offset. We recalibrate our sample for this offset by creating a pipeline-corrected redshift,

$$z_{\text{pipeline\_corr}} = z_{\text{pipeline}} + \langle z_{\text{Mg II}} - z_{\text{pipeline}} \rangle, \quad (\text{A1})$$

for which we recover a small offset of  $\sim 2.77 \times 10^{-3}$  ( $\sim 361 \text{ km s}^{-1}$  at  $z \sim 2.3$ ).

Employing this BOSS pipeline-corrected redshift, we perform the full analysis as performed within Sections 4 and 5. With respect to the covariance matrices, we recover effectively identical correlations amongst our line profile parameters. In order to better gauge the performance of these two possible samples, we recover the fraction of QSOs with a reconstructed flux recovered to within 15 per cent at both 1205 and 1220 Å (see e.g. Fig. 11). Though the differences are minor, we find that the original BOSS pipeline

redshift ( $z_{\text{pipeline}}$ ) performs marginally better than  $z_{\text{pipeline\_corr}}$ . At 1205 Å, we recover the QSO flux to within 85 (82) per cent for  $z_{\text{pipeline}}$  ( $z_{\text{pipeline\_corr}}$ ) and 90 (88) per cent at 1220 Å.<sup>18</sup> Given that the primary aim of this work is to reconstruct Ly $\alpha$  emission profiles, then the most natural choice for a redshift estimate is the one that performs best at this reconstruction; the line parameter correlations are a secondary product. Therefore, we conclude that owing to the marginally improved statistics on the recovery of the QSO flux from the  $z_{\text{pipeline}}$  sample relative to  $z_{\text{pipeline\_corr}}$  and the reasons mentioned previously for not considering other redshift estimates, the best redshift to adopt within this work is  $z_{\text{pipeline}}$ .

## APPENDIX B: PREFERENCE FOR THE NUMBER OF GAUSSIAN COMPONENTS FOR A LINE PROFILE

In the construction of our covariance matrix in Section 4.1, we model the Ly $\alpha$  and C IV emission lines as a double component Gaussian, whereas for the Si IV + O IV] and C III] lines, we consider only a single component Gaussian. In this appendix, we detail quantitatively the reasoning for our choices. To objectively differentiate between the various combinations, we use the Bayes information criterion (BIC; Schwarz 1978; Liddle 2004). The BIC can be computed using,

$$\text{BIC} = -2 \ln(\mathcal{L}) + k \ln(N), \quad (\text{B1})$$

where  $\mathcal{L}$  is recovered from the  $\chi^2$  fit to the individual emission-line profile,  $k$  is the number of free parameters and  $N$  is the number of available data points. A lower recovered BIC for an individual fit to the emission-line profile is considered to be a better characterization of the line.

The comparison between two possible sets of parameters to describe the emission-line profile can be quantitatively described by the difference in the two BICs,  $\Delta\text{BIC}$ . A recovered  $\Delta\text{BIC} > 10$  provides very strong evidence for the model with the lower BIC, whereas for  $6 < \Delta\text{BIC} < 10$ , strong evidence exists. Throughout this appendix, we discuss each emission-line profile individually and recover the  $\Delta\text{BIC}$  for each model to distinguish between our preferred choices.

### B1 The Ly $\alpha$ profile

For the Ly $\alpha$  emission-line profile, we consider the full emission-line complex within the rest-frame wavelength range  $\lambda = [1170, 1280] \text{ \AA}$ . This provides three different potential line species to be fit, Ly $\alpha$ , N V and the Si II line. Given the importance of the N V line for the full line complex, we always fit the N V line in addition to the Ly $\alpha$  line. Therefore, we consider four different combinations to potentially characterize the full Ly $\alpha$  line complex. First, we consider the Ly $\alpha$  line as a double component Gaussian, with a single component Gaussian each for the N V and Si II emission lines. Next, the same, but only a single component Ly $\alpha$  component. Finally, we consider these same two combinations excluding the Si II line.

In Table B1, we report the  $\Delta\text{BIC}$  for these four combinations of emission lines. We compute the BIC as outlined in equation (B1), recovering the  $\chi^2$  within the wavelength range  $\lambda = [1170, 1280] \text{ \AA}$ . In the construction of Table B1, we use the ‘conservative’ sample consisting of 2653 QSOs. We then recover the  $\Delta\text{BIC}$  from the difference between a model with a double component Gaussian

<sup>18</sup> For completeness, for  $z_{\text{Mg II}}$ , we recover the QSO flux to within 15 per cent for 80 per cent of the QSOs at 1205 Å and 85 per cent at 1220 Å.

**Table B1.** We use the Bayes information criterion (BIC) to distinguish whether the emission lines used within our covariance matrix should be fit with a single or a double component Gaussian. For each potential combination, we present the  $\Delta\text{BIC}$  to distinguish between very strong evidence ( $\Delta\text{BIC} > 10$ ) and strong evidence ( $6 < \Delta\text{BIC} < 10$ ) for a certain combination of lines (first column) relative to an alternative combination (second) column. See the text for further details regarding the various combinations of line profiles considered.

Line fitting type (preferred option)	Line fitting type (compared against)	QSOs with $\Delta\text{BIC} > 10$ (%)	QSOs with $6 < \Delta\text{BIC} < 10$ (%)
$\text{Ly}\alpha$ double component, N v and Si II	$\text{Ly}\alpha$ double component and N v	60.9	1.1
$\text{Ly}\alpha$ double component, N v and Si II	$\text{Ly}\alpha$ single component, N v and Si II	79.4	0.7
$\text{Ly}\alpha$ double component, N v and Si II	$\text{Ly}\alpha$ single component and N v	93.0	0.4
Si IV +O IV] single component	Si IV +O IV] double component	64.7	6.9
C IV double component	C IV single component	94.0	0.3
C III] single component and Al III	Only C III] double component	53.8	2.9
C III] single component and Al III	C III] double component and Al III	45.7	6.3
C III] single component and Al III	Only C III] single component	92.2	0.9

for  $\text{Ly}\alpha$  and the single components for N v and Si II. It is clear from this table that this is the preferred choice for modelling the  $\text{Ly}\alpha$  line complex. Importantly, we find strong evidence for a double component  $\text{Ly}\alpha$  emission line in over 80 per cent of the QSOs we consider. In principle, we could have explored whether further components for the  $\text{Ly}\alpha$  line are preferred; however, for the sake of simplicity, we have refrained from doing so. Furthermore, while the Si II emission line is typically only a weak ionization line, and in some cases not resolved within individual QSOs, we still find strong evidence for its inclusion in the QSO fitting (preferred in  $\sim 62$  per cent of our sample).

### B2 The Si IV +O IV] profile

Unlike the  $\text{Ly}\alpha$  line considered above, the blended Si IV +O IV] doublet is a strong, isolated emission line. We therefore consider the simplified choice of whether a single or double component Gaussian is preferred for this line within the wavelength range  $\lambda = [1360, 1440]$  Å. From Table B1, we find that a single component Gaussian is very strongly preferred at  $\sim 65$  per cent, which becomes  $\sim 72$  per cent when the criteria is lowered to only strong evidence.

### B3 The C IV profile

For the C IV doublet, we consider the emission-line complex within the wavelength range,  $\lambda = [1500, 1600]$  Å. Again, the C IV emission line is an isolated, very strong high-ionization line, therefore we only need to consider whether a single or double component Gaussian is preferred. In Table B1, we recover very strong evidence for the choice of a double component Gaussian, with this being preferred 94 per cent of the time.

### B4 The C III] profile

The C III] emission line is not an isolated line, instead it is the strongest line in a complicated emission line profile (e.g. Vanden Berk et al. 2001). Surrounding the C III] line are the contributions from the Fe pseudo-continuum, as well as contributions from the Al III and Si III] line. In this work, we consider the contribution of the Fe pseudo-continuum to be negligible to the C III] line and for all intents and purposes, we additionally consider the Si III] contribution negligible. This latter point arises from the insufficient S/N of these BOSS QSOs to fully resolve and separate out this line contribution. While it may be present in the highest S/N QSOs in our sample, for the vast majority, it cannot be easily distinguished. Furthermore,

from Vanden Berk et al. (2001), the relative line fluxes differ by over a factor of 100.

We consider four scenarios to characterize the C III] line complex. A double component C III] line in combination with a single component Gaussian for Al III, a single component C III] and Al III line, and then just a single or double component Gaussian for the C III] line, without considering the Al III line. In Table B1, we find just a single C III] emission line to be very strongly disfavoured with respect to a single component C III] and Al III ( $\sim 92$  per cent). However, in the case of the remaining scenarios, it is not as clear.

Comparing the single C III] and Al III components to a purely double component C III] (no Al III), we find marginally stronger evidence for the single C III] scenario (preferred  $\sim 54$  per cent of the time). However, note that in allowing for a double component C III], these two scenarios are effectively the same. For example, the broad component can just fit the Al III line, leaving a single C III] line. This degeneracy therefore tends to draw these two scenarios to be more equally preferred. As a result, the single C III] and Al III scenario is considered to be preferable.

In the case of comparing a single or double component C III] line in combination with Al III, we find comparable results for the  $\Delta\text{BIC}$ . Between these two scenarios, we find a single component very strongly preferred in  $\sim 46$  per cent of the QSOs sampled, which increases to  $\sim 52$  per cent if we lower the criteria to just strong evidence. It is therefore not immediately clear from the  $\Delta\text{BIC}$  which is the preferred fitting scenario to consider for the C III] line complex. As a result, we choose to consider a single C III] component with a Al III contribution purely on the grounds of there being less model parameters, removing potential degeneracies between a broad and narrow component C III] from our covariance matrix.

## APPENDIX C: QSO QUALITY ASSESSMENT EXAMPLES

In Section 3.5, we briefly outlined the visual quality assessment we performed to obtain the two QSO samples for the covariance matrix. Within this appendix, we provide a more detailed explanation of the respective criteria we consider, as well as providing a select few examples that best indicate the various decisions that we have made.

### C1 Removal of QSOs

The first step of our quality assessment was the removal of any QSOs from which we recovered a poor characterization of the QSO

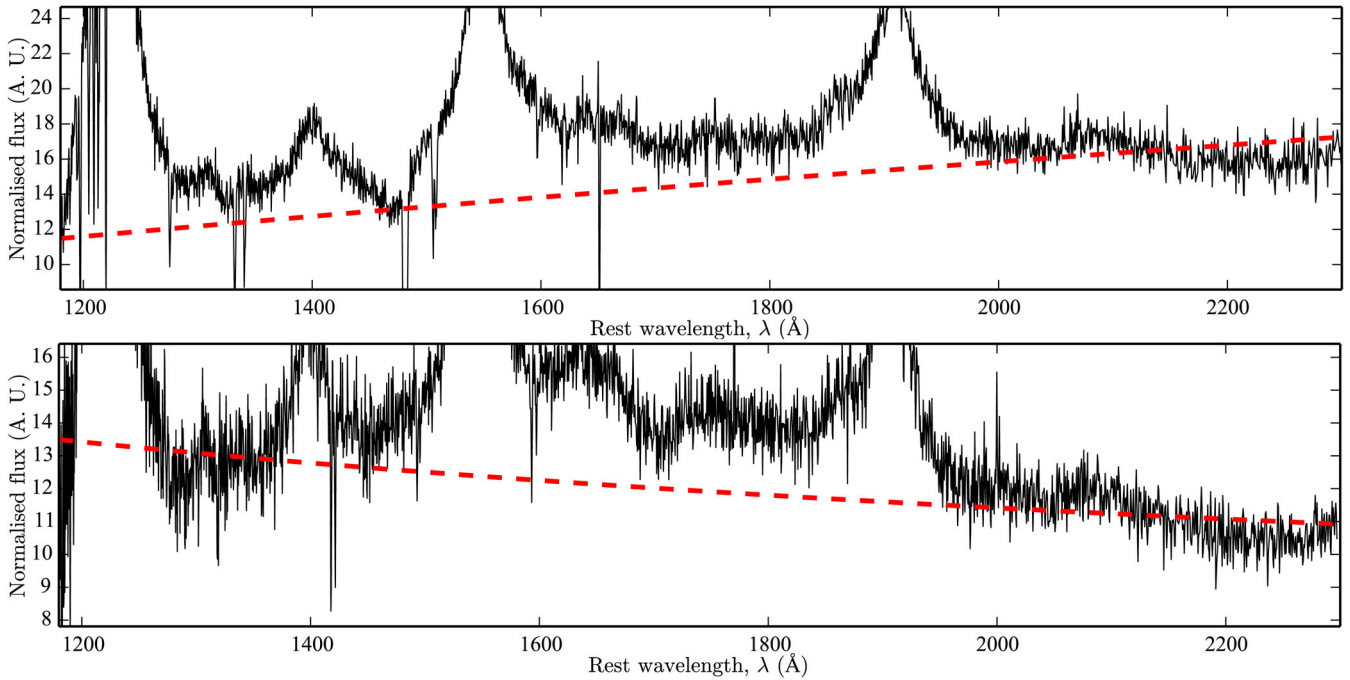


**Figure C1.** Representative examples of QSOs removed from our samples due to continuum estimation issues. Top panel: the recovery of a positive QSO continuum spectral index ( $f_{\lambda} \propto \lambda^{\alpha_{\lambda}}$ ). A small number of QSOs contain a positive spectral index, counter to the vast majority of QSOs that have a negative spectral index. Bottom panel: a QSO continuum where a single power-law continuum cannot fit the observed spectrum. In this example, a two component continuum with a break near C IV would improve the fit. Only a rare few QSOs show this behaviour, therefore there is no motivation to retain them. Note that  $1 \text{ au} = 10^{-17} \text{ erg cm}^{-2} \text{ s}^{-1} \text{ \AA}^{-1}$ .

continuum. In Fig. C1, we provide two examples of QSOs that were removed failing this criteria. In the top panel, the recovered QSO returns a positive spectral index,  $\alpha_{\lambda}$ , which is counter to the negative spectral indices recovered by the vast majority of our QSO sample. The recovery of a positive spectral index is unphysical and likely arises from flux calibration errors. Only a few QSOs within our sample are found to have a positive spectral index. In the bottom panel of Fig. C1, we provide an example of a QSO where a single power law is insufficient to characterize the QSO continuum within our fitting region. To adequately characterize this QSO, a double component continuum pivoting on C IV would be required. The rarity in recovering such an object likely points to this being an error in the data reduction pipeline, or the flux calibration.

The next step in our visual QSO quality assessment is the removal of any QSO spectra that have either (i) missing sections of the observed QSO flux that overlap with our chosen emission lines, (ii) a large number of absorption features, (iii) either an intervening dense neutral absorber or sufficiently strong/broad absorption blueward of C IV or (iv) an Ly $\alpha$  line region that is not well fit or characterized by our MCMC pipeline. In Fig. C2, we present nine examples of QSOs removed from our sample. We discuss each one of these QSOs below.<sup>19</sup>

(1) A clear, dense neutral absorber in the direct vicinity of the QSO. Presence of the neutral absorber completely removes any ability to recover an Ly $\alpha$  broad component.

<sup>19</sup> Note that in Figs C2–C4, we represent the corresponding fitted absorption profiles as being subtracted from the continuum flux level rather than the true flux level. As a result, in some cases, it appears that the absorption extends to negative flux. However, this choice is purely to aid the visual representation of the full emission profile fits.

(2) Two strong absorption features near Ly $\alpha$ . The first, blueward of Ly $\alpha$ , removes almost half of the Ly $\alpha$  line. Even in the presence of this absorber, the intrinsic Ly $\alpha$  line profile recovery is still reasonably good. However, it still underpredicts the true profile. Furthermore, absorption on the N v line centre removes any ability to recover the N v line, resulting in a much broader Ly $\alpha$  component than should be recovered.

(3) Strong Ly $\alpha$  absorption at the line centre. Without a sufficient fraction of the Ly $\alpha$  line centre, the intrinsic Ly $\alpha$  line cannot be recovered. While a broad Ly $\alpha$  component can still be estimated, no narrow component can be reliably obtained.

(4) Another, even more extreme example of strong absorption on Ly $\alpha$  line centre. Presence of several strong Ly $\alpha$  absorption features completely removes any information to obtain the Ly $\alpha$  narrow-line component.

(5) A Ly $\alpha$  line profile with no prominent narrow-line component. As a result, the two Gaussian components both prefer to be broad and are therefore degenerate. The absorption on line centre likely contaminated the Ly $\alpha$  peak determination leading to the two preferred degenerate broad components.

(6) A large, connected series of narrow absorption features centred on Ly $\alpha$ . Since the entire Ly $\alpha$  profile is contaminated by absorption, measuring the Ly $\alpha$  narrow component peak amplitude becomes degenerate with the depth of the absorption features.

(7) The MCMC pipeline struggles to recover the extremely narrow, sharp peak around Ly $\alpha$  line centre. Evidence of two small absorption features (which are not identified by our algorithm) on either side of line centre appear to cause this peak to become too narrow to fit.

(8) Significant blueward absorption features near the C IV line contaminates the recovery of the broad component. Not a BAL QSO,

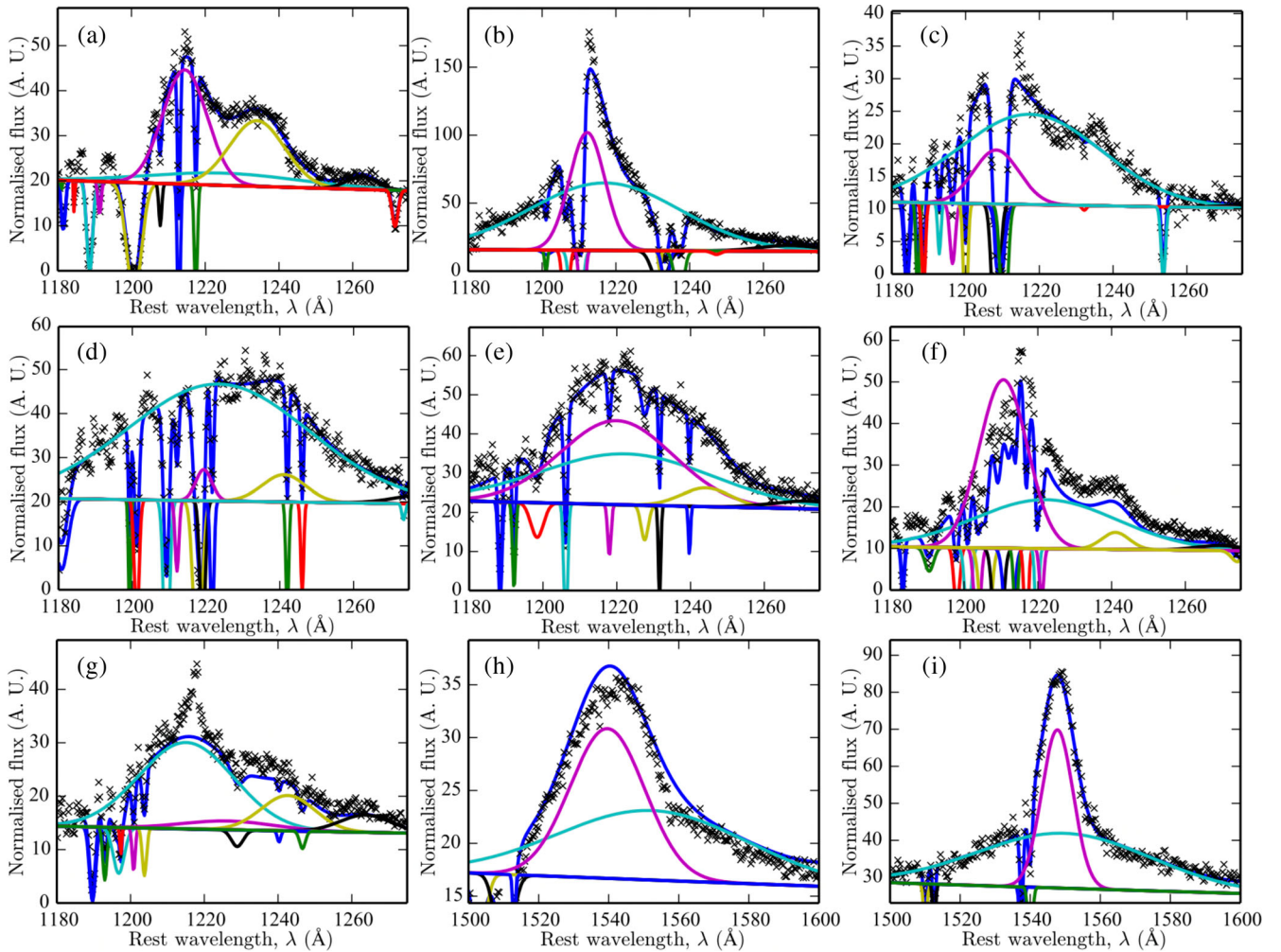


**Figure C2.** Representative examples of QSOs removed from our samples due to a variety of issues. Top left: intervening strong Ly $\alpha$  absorber. Top centre: strong Ly $\alpha$  absorption offset from line centre impacting the intrinsic profile recovery. Top right: strong Ly $\alpha$  absorption at line centre. Middle left: a substantial number of Ly $\alpha$  absorption features contaminating the Ly $\alpha$  emission-line profile. Middle centre: no prominent Ly $\alpha$  emission profile. Middle right: significant Ly $\alpha$  line absorption that becomes degenerate with the Ly $\alpha$  emission-line profile. Bottom left: the MCMC algorithm is unable to fit the intrinsic Ly $\alpha$  profile owing to absorption impacting the Ly $\alpha$  emission-line profile. Bottom centre: C IV absorption in the line wing, impacting the broad component determination. Bottom right: small C IV absorption feature that artificially prefers a narrower line component than should be recovered.

however, the absorption features are still sufficient to contaminate the recovery of the full line profile.

(i) Deep, narrow absorption features on the C IV line profile. The unfortunate location of these features at the wing of the C IV narrow component causes a narrower C IV line than should be expected. The depth of these features causes this behaviour, weaker absorption would not impact the narrow component recovery.

### C2 Examples of QSOs in the ‘conservative’ sample

In Fig. C3, we provide three examples of QSOs that are classified as ‘conservative’ only (not considered for the ‘good’ sample). In the first example (left-hand panel), several strong narrow absorption features are detected and fit. These are offset from the line centre of Ly $\alpha$ , allowing the peak height of Ly $\alpha$  to still be reliably estimated. Though the intrinsic profile appears to be well recovered, the uncertainties in the peak amplitude owing to potential degeneracies with the relative strengths of the absorption features and the number of identified absorption features causes this to be only characterized as ‘conservative’.

The second example (middle panel) has a strong absorption feature on Ly $\alpha$  line centre. However, the relative strength of this feature is not sufficient to completely contaminate the peak of the Ly $\alpha$  line (unlike similar examples in Fig. C2). It appears that the full Ly $\alpha$  line profile is recovered well, despite numerous narrow absorption features and the strong central absorption. The uncertainties surrounding the narrow Ly $\alpha$  component determination from the strong absorption results in its assessment as ‘conservative’ only. Finally, in the last example (right-hand panel), the full Ly $\alpha$  line profile is contaminated by a large number of narrow absorption features. None of these are located at line centre, nor do they appear to impact the recovery of the Ly $\alpha$  line profile. However, the sheer number of features causes this QSO to be classified as conservative.

### C3 Examples of QSOs in the ‘good’ sample

Finally, in Fig. C4, we present three examples of QSOs explicitly selected for our refined ‘good’ sample (all QSOs in the ‘good’ sample appear in the ‘conservative’ sample). In the first example (left-hand panel), there are only a few very small absorption features. In the

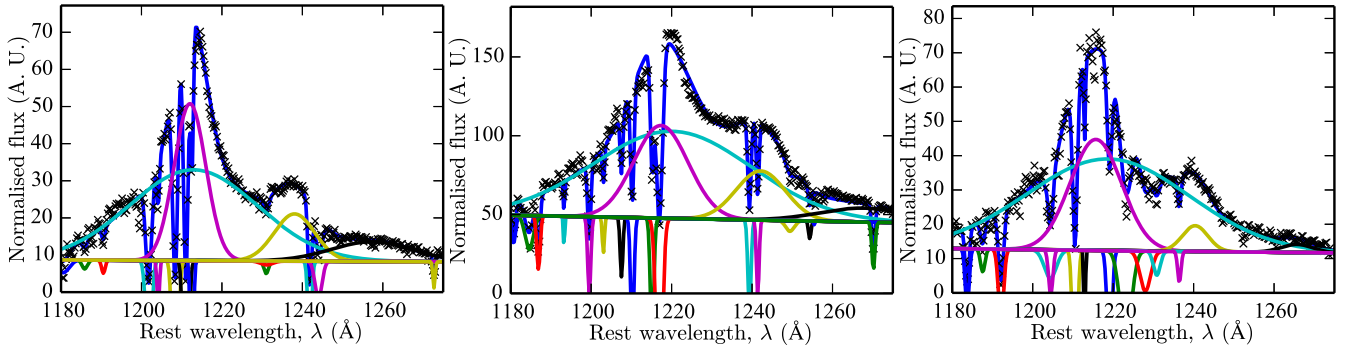


**Figure C3.** Representative examples of Ly $\alpha$  profiles that are classified in the ‘conservative’ sample (more uncertainty in the recovery of the intrinsic Ly $\alpha$  profile). Left-hand panel: a large number of clustered absorption lines blueward of Ly $\alpha$  that are identified and well fit. The pristine red side of the Ly $\alpha$  line should enable the intrinsic Ly $\alpha$  profile to be well characterized. Centre panel: a large number of absorption lines that are well fit and characterized. The broader Ly $\alpha$  absorption feature will likely impact the recovery of the intrinsic profile, but there is still sufficient evidence that the intrinsic Ly $\alpha$  profile might be well estimated. Right-hand panel: a large number of absorption features on both the blue and red side of Ly $\alpha$ . The absence of line centre absorption should enable the intrinsic profile to be recovered with some small uncertainty.

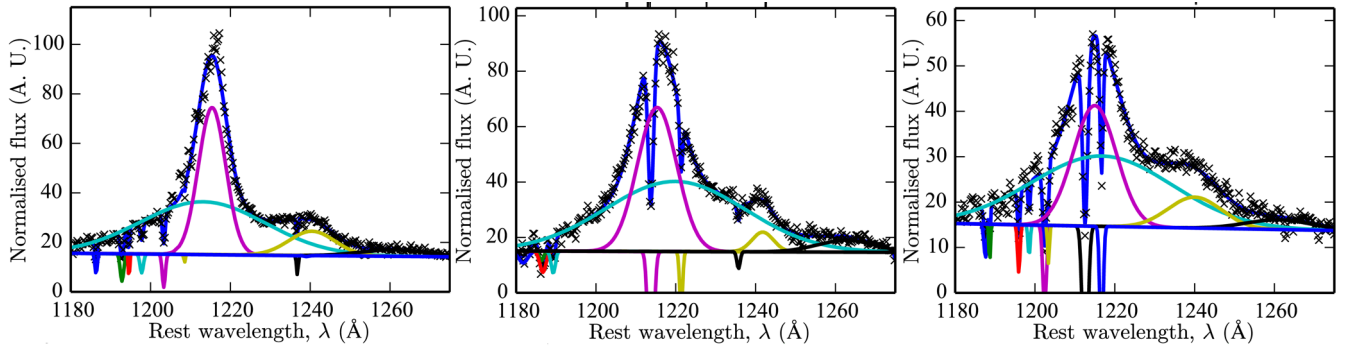


**Figure C4.** Representative examples of Ly $\alpha$  profiles that are classified in the ‘good’ sample. Left-hand panel: the absence of any absorption. Centre panel: small absorption, offset from the centre of Ly $\alpha$ . These features are identified and fit and therefore do not impact on the ability to fit the intrinsic Ly $\alpha$  profile. Right-hand panel: a larger number of absorption feature, all identified and well fit. The narrow width of the absorption features around Ly $\alpha$  should not impact the fitting of the Ly $\alpha$  profile.

absence of anything stronger, these QSOs are classified as ‘good’. The second example (middle panel), once again, has very few absorption features. Despite being strong, narrow absorption lines, these are well characterized and do not impact the recovery of the intrinsic Ly $\alpha$  line at all. In the final example (right-hand panel), a larger number of absorption lines are present. Importantly though, these are located offset from the Ly $\alpha$  line centre and therefore we are confident that the true profile is recovered. Note that this profile is similar to the first example in Fig. C3. The reason this QSO is classified as ‘good’ and the previous was ‘conservative’ arises from the number of absorption lines. In this example, only two narrow features impact the Ly $\alpha$  line, whereas in the previous case, several lines have resulted in a smaller fraction of the total Ly $\alpha$  profile being unaffected by the absorption features. Ultimately, this is only a minor difference that does not change any of the conclusions of this work, since in Section 4.4, we found similar correlation matrices between the two samples.

#### APPENDIX D: RECOVERY OF CONTINUUM PARAMETERS FROM $\lambda > 1275 \text{ \AA}$

In Section 5.2, we alluded to an assumption regarding the usage of the QSO continuum between the full MCMC fitting and the reconstruction profile fitting. Specifically, we assume that the

continuum measured from an Ly $\alpha$  obscured or high- $z$  QSO in the region ( $\lambda > 1275 \text{ \AA}$ ) will be equivalent to the continuum recovered from fitting the full QSO within the range  $1180 \text{ \AA} < \lambda < 2300 \text{ \AA}$ . However, by not fitting in the  $1180 \text{ \AA} < \lambda < 1275 \text{ \AA}$  region, we could be losing information from the Ly $\alpha$  line profile (and surrounding region) that could be otherwise used to refine the estimate of the QSO continuum. Of course, this cannot be tested on an actual QSO that requires reconstruction, but instead, we can statistically test this assumption across the full QSO sample we have used within this work.

In Fig. D1, we present the 2D scatter of the two QSO continuum parameters, the continuum flux amplitude normalized to  $1450 \text{ \AA}$  ( $f_{1450}$ , left-hand panel) and the spectral index,  $\alpha_\lambda$  (right-hand panel). To facilitate the comparison, the red dashed curve corresponds to the one-to-one relation. Note that while the flux amplitude is normalized at  $1450 \text{ \AA}$ , which should be unaffected by the different fitting regions, we allow a perturbation on this flux to refine its true normalization. In the case of this continuum normalization, we find very little scatter and all QSOs lie along the one-to-one relation indicative of there being no adverse effects from this assumption.

In the case of the QSO spectral index, we again find all QSOs to essentially lie perfectly along the one-to-one relation. However, in several instances, there are QSOs that deviate away from this line. This small scatter indicates that for a select few QSOs, fitting in the  $1180 \text{ \AA} < \lambda < 1275 \text{ \AA}$  region is important for the recovery of

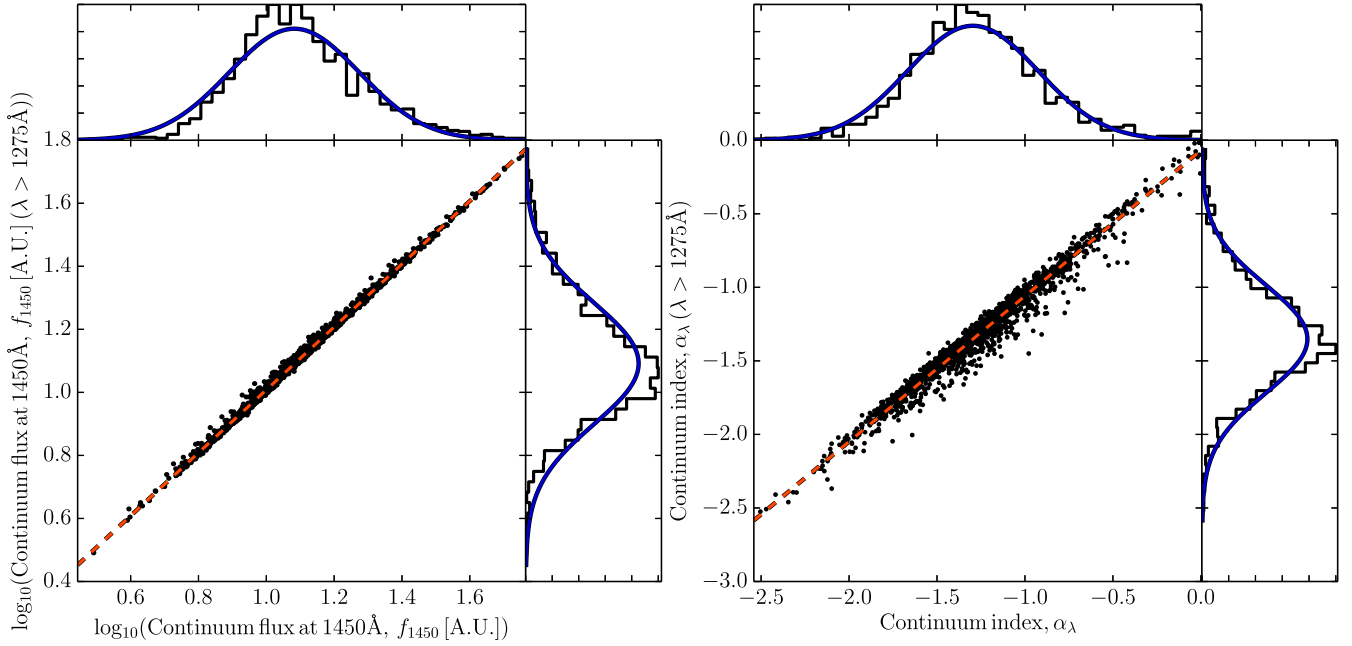


**Figure D1.** 2D scatter plots comparing the estimation of the two continuum parameters between the full MCMC fit and the Ly $\alpha$ -masked QSO fit for reconstruction (masked at  $\lambda < 1275 \text{ \AA}$ ). Left-hand panel: the continuum flux normalized at  $1450 \text{ \AA}$ ,  $f_{1450}$ . Right-hand panel: the continuum spectral index,  $\alpha_\lambda$ . The red dashed curve corresponds to the one-to-one relation. There is very little scatter about the one-to-one relation, indicating that there are no biases in the estimation of the continuum parameters when fitting either the full QSO or fitting at  $\lambda > 1275 \text{ \AA}$ . Note that  $1 \text{ au} = 10^{-17} \text{ erg cm}^{-2} \text{ s}^{-1} \text{ \AA}^{-1}$ .

the true continuum spectral index. Importantly, around Ly $\alpha$  even for the extreme QSOs in this 2D plot, the level of discrepancy in the continuum flux will be at most 10 per cent. Furthermore, this is purely for the continuum flux and not the total line flux. Referring to Fig. 9, a 10 per cent error on the continuum flux at Ly $\alpha$  will fall well within the errors of the reconstructed Ly $\alpha$  emission-line profile. Therefore, within the model uncertainties of the Ly $\alpha$

reconstruction pipeline, this scatter is not significant to drastically affect the reconstructed Ly $\alpha$  line profile and hence the assumption on using the same QSO continuum is justified.

This paper has been typeset from a  $\text{T}_{\text{E}}\text{X}/\text{L}^{\text{A}}\text{T}_{\text{E}}\text{X}$  file prepared by the author.